Journal of Materials Chemistry A

ROYAL SOCIETY OF CHEMISTRY

PAPER

View Article Online
View Journal | View Issue

Cite this: J. Mater. Chem. A, 2024, 12, 26645

The aerosol-assisted chemical vapour deposition of Mo-doped $BiVO_4$ photoanodes for solar water splitting: an experimental and computational study†

Shaobin Zhao,[a] Chenglin Jia,[b] Xinyi Shen,[a] Ruohao Li,[a] Louise Oldham,[a] Benjamin Moss,[a] Brian Tam,[ac] Sebastian Pike,[d] Nicholas Harrison,[ae] Ehsan Ahmad*[ae] and Andreas Kafizas*[af]

$BiVO_4$ is one of the most promising light absorbing materials for use in photoelectrochemical (PEC) water splitting devices. Although intrinsic $BiVO_4$ suffers from poor charge carrier mobility, this can be overcome by Mo-doping. However, for Mo-doped $BiVO_4$ to be applied in commercial PEC water splitting devices, scalable routes to high performance materials need to be developed. Herein, we propose a scalable aerosol-assisted chemical vapour deposition (AA-CVD) route to high performance Mo-doped $BiVO_4$. The materials were characterised using X-ray diffraction (XRD), Raman spectroscopy, X-ray photoelectron spectroscopy (XPS), scanning electron microscopy (SEM), atomic force microscopy (AFM), UV-visible absorption spectroscopy, and a range of PEC tests. By studying a range of Mo-precursor doping levels (0 to 12% Mo : V), an optimum precursor doping level was found (6% Mo : V); substituting V^{5+} sites in the host structure as Mo^{6+}. In PEC water oxidation the highest performing material showed an onset of photocurrent (J_{on}) at ~0.6 V_{RHE} and a theoretical solar photocurrent (TSP) of ~1.79 mA cm^{-2} at 1.23 V_{RHE} and 1 sun irradiance. Importantly, Mo-doping was found to induce a phase change from monoclinic clinobisvanite (m-$BiVO_4$), found in undoped $BiVO_4$, to tetragonal scheelite (t-$BiVO_4$). The effect of Mo-doping on the phase stability, structural and electronic properties was examined with all-electron hybrid exchange density functional theory (DFT) calculations. Doping into V and Bi sites at 6.25 and 12.5 at% was calculated for t-$BiVO_4$ and m-$BiVO_4$ phases. In accord with our observations, 6.25 at% Mo doping into the V sites in t-$BiVO_4$ is found to be energetically favoured over doping into m-$BiVO_4$ (by 2.33 meV per Mo atom inserted). The computed charge density is consistent with n-doping of the lattice as Mo^{6+} replaces V^{5+} generating an occupied mid-gap state ~0.4 eV below the conduction band minimum (CBM) which is primarily of Mo-4d character. Doubling this doping level to 12.5 at% in t-$BiVO_4$ resulted in the mid-gap state merging with the CBM and the formation of a degenerate semiconductor with electrons distributed over the 3d orbitals of V ions residing in the [001] plane. In conjunction with our experimental findings, this strongly suggests that it is the increased electron conductivity due to Mo doping of $BiVO_4$ that produces a more active photoanode for water splitting, and that this maximises between 6.25 to 12.5 at% doping.

Received 16th April 2024
Accepted 5th September 2024

DOI: 10.1039/d4ta02605e

rsc.li/materials-a

1 Introduction

Since the industrial revolution, societal dependence on fossil fuels has grown exponentially, which has caused CO_2 levels in the atmosphere to rise from ~280 ppm in ~1750 to ~410 ppm today.[1,2] This dramatic rise in CO_2 levels is the primary cause of climate change, which may have potentially catastrophic impacts if not curtailed.[3,4] In order to reduce CO_2 emissions,

[a]Department of Chemistry, Molecular Science Research Hub, Imperial College London, White City, London, W12 0BZ, UK. E-mail: ehsan.ahmad08@imperial.ac.uk; a.kafizas@imperial.ac.uk

[b]Department of Chemistry, University College London, 20 Gordon Street, London, WC1H 0AJ, UK

[c]Department of Physics, Imperial College London, South Kensington, London, SW7 2AZ, UK

[d]Department of Chemistry, University of Warwick, Coventry, CV4 7AL, UK

[e]Thomas Young Centre, The London Centre for the Theory and Simulation of Materials, Royal School of Mines, Imperial College London, South Kensington, London, SW7 2AZ, UK

[f]London Centre for Nanotechnology, Imperial College London, South Kensington, London, SW7 2AZ, UK

† Electronic supplementary information (ESI) available. See DOI: https://doi.org/10.1039/d4ta02605e

various renewable routes to fuels have been developed, where artificial approaches that can split water and produce H_2 fuel have shown the most promise in terms of conversion efficiency.[5] Of the various materials that have demonstrated the ability to drive this process,[6–8] bismuth vanadate ($BiVO_4$) has emerged as one of the most promising candidates for commercial applications given its high performance,[9] long-term stability,[10] and ease of fabrication.[11,12]

Nevertheless, in order for $BiVO_4$ to be applied in commercial water splitting devices, scalable synthetic routes must be developed. To address this challenge, herein, we develop a new chemical vapour deposition (CVD) based route – a method used by industry to grow coatings at scale[13] – to grow high performance $BiVO_4$ for applications in water splitting. Sagu *et al.* used an aerosol-assisted CVD (AA-CVD) method to produce monoclinic $BiVO_4$ (m-$BiVO_4$) from the reaction of bismuth nitrate pentahydrate and vanadyl acetylacetonate, carried in a methanol solvent using air, at 500 °C and 1 atm.[14,15] Ager *et al.* used a vapour transport CVD (VT-CVD) method to produce m-$BiVO_4$ from the reaction of bismuth metal and vanadium pentoxide vapours carried in air at ~460 °C and ~0.01 atm.[16] Gupta *et al.* used a direct liquid injection CVD (DLI-CVD) method to produce m-$BiVO_4$ from the reaction of vanadyl acetylacetonate and triphenyl bismuth, carried in a dimethyl formamide solvent using Ar : O_2 gas, at ~550 °C and ~0.001 atm.[17] Herein, we develop a new AA-CVD route to produce phase-pure m-$BiVO_4$ from the reaction of vanadyl acetylacetonate and triphenyl bismuth, carried in an acetone/methanol solvent mixture (3 : 1) using air, at 400 °C and 1 atm.

Intrinsic $BiVO_4$ possesses a number of properties that make it a good choice for applications in photoelectrochemical water splitting.[18,19] These include a visible light bandgap (~2.4 eV), which allows the material to harvest ~10.9% of the solar spectrum, and in theory, achieve a solar-to-hydrogen (STH) efficiency of ~9.1%. This is almost in line with the recommended minimum STH (10%) that should be achieved for water splitting devices to be considered economically viable.[20] $BiVO_4$ also possesses intrinsic n-type conductivity,[21] and a strongly oxidising valence band (+~2.5 V_{RHE}),[22] making it ideal for applications as a photoanode to drive the water oxidation half reaction (+1.23 V_{RHE}). However, $BiVO_4$ also possesses intrinsic properties that can limit its water splitting performance. This includes its comparatively fast intrinsic electron–hole recombination dynamics (full recombination by ~ms timescale with no applied bias[23]) in comparison to the kinetics in which it can drive water oxidation (~100 ms).[24,25] Another caveat is its relatively short electron carrier diffusion length (as low as ~10 nm),[26] which unless resolved, will severely limit electron extraction from the material; resulting in high levels of recombination.[27] Nevertheless, this issue can be overcome by increasing the conductivity of $BiVO_4$, which is often achieved by impurity doping; with W or Mo substitution of V sites thus far showing the most promise.[28,29] The rationale for the success of this strategy lies in the ability of these dopants to insert in their hexavalent form,[30–32] and thereby act as a source of electron donors to the crystal.[33] In this work, Mo-doped $BiVO_4$ is studied, and the Kröger–Vink notation for its substitution of vanadium is shown below:

$$Mo_V^{\times} \rightleftharpoons Mo_V^{\bullet} + e^- \quad (1)$$

Mo-doped $BiVO_4$ can be grown using a range of synthetic methods, including electrodeposition,[34–36] electrospinning,[30,31] electrostatic spray deposition (ESD),[32] metal–organic deposition[37–41] and physical vapour deposition (PVD).[42,43] Herein, we develop a one pot AA-CVD route to Mo-doped $BiVO_4$. The inherent scalability of this route, coupled with the simplicity of this method (ambient pressure and moderate temperature) makes this method an attractive option for the potential industrial-production of Mo-doped $BiVO_4$-based devices.

Herein, a range of Mo precursor doping levels were studied (from 1 to 12% Mo : V), resulting in the formation of Mo-doped $BiVO_4$ films with doping levels from 2.0 to 12.7% Mo : V. A ~9.6% Mo : V doping level was found to produce the most active photoanodes for driving the water oxidation reaction; showing theoretical solar photocurrents (TSPs) of up to 1.79 mA cm^{-2} at 1.23 V_{RHE}. Intriguingly, Mo-doping was found to induce a phase transition in the $BiVO_4$ host, partially distorting the structure from its less symmetric monoclinic form to more symmetric tetragonal form (t-$BiVO_4$). Despite t-$BiVO_4$ often showing lower levels of photocatalytic activity than m-$BiVO_4$,[44,45] herein the opposite effect was seen, which we attribute to the beneficial electronic effects of introducing Mo into the host structure. It should be noted that this phase change is caused by relatively small changes in atomic positions, resulting only in subtle changes in the XRD pattern. Upon reviewing the literature on Mo-doped $BiVO_4$, we see that the possibility for this change in crystal structure is rarely discussed,[34,37] and on occasion, there may have been cases where the crystal structure was incorrectly deemed as being monoclinic when the tetragonal structure was more likely present. Herein, the Mo-doping induced phase transition for the range of samples produced (2.0 to 12.7% Mo : V) is studied using XRD and Raman spectroscopy.

All electron, hybrid exchange density functional theory calculations have been used to examine the phase change induced by Mo-doping and the associated changes in electronic structure. An accurate description of exchange and on-site electronic correlation is essential if the spatial delocalisation, spin polarisation and energy of the d-orbitals are to be reproduced.[46,47] Electronic exchange and correlation were therefore approximated using the hybrid PBE0 functional.[48] This functional has demonstrated an improvement over local density functional theory (DFT) functionals in strongly correlated systems in both describing the character of electronic bands and in the prediction of band gaps, the latter of which are systematically underestimated with local DFT functionals due to their in-built self-interaction.[49] In this study, however, we have opted for a reduced 10% mixing of Hartree–Fock (HF) exchange (PBE0-10) as the band gaps in strongly correlated materials are observed to be overestimated at the standard 25% mixing of PBE0.[50,51] To the authors knowledge, this is the first study to have applied this approach to Mo doping in both the t-

$BiVO_4$ and m-$BiVO_4$ structures. The calculations herein document the effects of Mo doping on the phase stability, local structure, projected density of states (PDOS) and bandgap, and the spin density distribution of the n-doped charge density.

2 Experimental

2.1. Synthesis

Phase pure $BiVO_4$ coatings were grown on FTO glass substrates (TEC 15; 2.5 × 2.7 cm) using a novel aerosol-assisted chemical vapour deposition (AA-CVD) method, inside a cold wall reactor (Fig. S1†). Substrates were heated from underneath using a graphite heating block. The inlet to the reactor was equipped with a cooling water jacket to prevent any prior decomposition of the precursor before reaching the reactor.

The precursor solution contained vanadyl acetylacetonate (0.056 g, 0.20 mmol), triphenyl bismuth (0.088 g, 0.20 mmol) in an acetone/methanol mixture (3 : 1; 40 ml). The solution was sonicated for 1 min to dissolve the precursors (VWR ultrasonic cleaner, 30 W, 45 kHz). The solution was then aerosolized using an ultrasonic humidifier (2 MHz, Liquifog, Johnson Matthey) and carried over the heated FTO substrate (400 °C) using compressed air at a flow rate of 5000 sccm (MFC, Brooks) over a period of ~20 min until the solution was fully transferred. To avoid unnecessary oxidation and change of the precursor solution, it was made fresh once the CVD reactor had reached temperature, and transferred immediately, with a total time from the making of the precursor solution to its transfer of less than 30 min.

A series of Mo-doped $BiVO_4$ coatings were made by adding molybdenum hexacarbonyl to the precursor solution before sonication. 1, 3, 6 and 12% Mo-doped $BiVO_4$ coatings were made by respectively adding 0.0005, 0.0015, 0.003 and 0.006 g (0.002, 0.006, 0.012, 0.024 mmol) to the precursor solution. The Mo-doping level represented the % Mo added with respect to the Bi (or V) precursor present in the precursor solution. All samples were subsequently annealed in an oven at 500 °C in air for 12 hours.

2.2. Physical characterisation

The speciation of the precursor solution was analysed using ^{1}H and ^{51}V NMR spectroscopy (Bruker Avance 600, 500 and 400 MHz instruments, with all chemical shifts reported in parts per million (ppm), ^{51}V NMR signals were reported against a $VOCl_3$ reference at 0 ppm). Chemical changes were monitored over time using visible absorption spectroscopy (Shimadzu UV-2600i). X-ray diffraction (XRD) patterns were measured with a Bruker D2 Phaser diffractometer with parallel beam optics equipped with a Lynx-Eye detector. X-rays were generated using a Cu source ($V = 30$ kV, $I = 10$ mA) with Cu $K_{\alpha1}$ ($\lambda = 1.54056$ Å) and Cu $K_{\alpha2}$ radiation ($\lambda = 1.54439$ Å) emitted with an intensity ratio of 2 : 1. Patterns were collected between $10° \leq 2\theta \leq 60°$ with a step size of 0.0243°. Patterns were compared to standards from the Physical Sciences Data-Science (PSDS) database.[52] Lattice parameters and the average crystallite size of each sample was determined from a Le Bail model, which was fit to each diffraction pattern using GSAS-EXPGUI software.[53] Raman spectra were obtained using a Horiba LabRam Infinity equipped a helium-neon laser (633 nm, 25 mW). The system was calibrated to a silicon reference, and samples were analysed over the 200–1200 cm^{-1} range. Standards were acquired from RRUFF project database.[54] For scanning electron microscopy (SEM), 15 nm of chromium was deposited on samples by sputtering to prevent charging. Images were taken using a Zeiss Auriga Cross Beam microscope with a Schottky field emission gun using a 5 keV electron beam. Atomic force microscopy was performed using an Agilent 5500AFM system in tapping-mode to investigate the surface morphology of the thin films deposited on FTO-coated float glass. The resonant frequency of the cantilever was approximately 270 kHz and the force constant was 40 N m^{-1}. The scanning probe microscopy control software PicoView was used to record film topography and phase changes of 1 μm^2 and 10 μm^2 regions. The images were processed and analysed using Gwyddion software. X-ray photoelectron spectroscopy (XPS) was performed using a Thermo Scientific™ K-Alpha™ instrument. The instrument uses monochromated and micro-focused Al-K_α ($h\nu$ = 1486.6 eV) radiation to eject photoelectrons that are analysed using a 180° double-focusing hemispherical analyser with a 2D detector. A flood gun was used to minimize sample charging. Spectra were collected at 2 × 10^{-9} mbar base pressure. All samples were referenced to the C–C peak of adventitious carbon in the C 1s spectrum at a binding energy of 284.8 eV to correct for any charge that is not neutralised by the flood gun. After correction for the instrument transmission function using the Avantage software package, data was analysed using CASAXPS software.[55] Ultra-violet visible (UV-vis) transmission spectroscopy was performed on a Shimadzu UV-vis 2600 spectrophotometer equipped with an integrating sphere.

2.3. Photoelectrochemical water splitting

All photoelectrochemical analyses were carried out in a home-made PEEK cell with quartz windows. Analyses were carried out in 0.1 M phosphate buffer (0.05 M K_2HPO_4, 0.05 M KH_2PO_4; pH = 7) in Milli-Q-water (Millipore Corp., 18.2 MΩ cm at 25 °C). For all measurements, a three electrode configuration was used, with a Pt mesh counter electrode and a Ag/AgCl reference electrode in sat. $KCl_{(aq.)}$ (0.197 V_{NHE} at 25 °C; Metrohm). An Autolab potentiostat (PGSTAT12 with an FRA2 module) was used to apply voltage and measure currents. All applied voltages are reported *vs.* the reversible hydrogen electrode (V_{RHE}), converted using the Nernst equation:

$$V_{RHE} = V_{Ag/AgCl} + (0.0591 \times pH) + V^{\varnothing}_{Ag/AgCl} \quad (2)$$

where $V_{Ag/AgCl}$ is the applied potential *vs.* the reference electrode and $V^{\varnothing}_{Ag/AgCl}$ is the standard potential of the reference electrode.

The light source used to measure current–voltage (*JV*) curves and incident photon to current efficiency (IPCE) curves was an ozone-free xenon lamp (75 W, Hamamatsu) coupled to a monochromator (OBB-2001, Photon Technology International). The IPCE was calculated using the following equation:[56]

$$\mathrm{IPCE}(\%) = (I_{\mathrm{ph}} \times 1239.8)/(P_{\mathrm{mono}} \times \lambda) \times 100 \quad (3)$$

where I_{ph} is the photocurrent (mA cm^{-2}), 1239.8 is the multiplication of Planck's constant with the speed of light (eV nm), P_{mono} is the light power at a given wavelength (mW cm^{-2}) and λ is the wavelength of the monochromated light (nm). The power was measured using a ThorLabs PM100D Power Energy Meter equipped with a S120VC sensor.

The solar water splitting activity was calculated using IPCE measurements. This theoretical solar photocurrent (TSP) was determined by multiplying the IPCE with the AM1.5 solar spectrum, and converting this into a current:[57]

$$\mathrm{TSP}\left(\mathrm{mA\ cm}^{-2}\right) = \int_{E_{\mathrm{bg}}(\mathrm{nm})}^{280\ \mathrm{nm}} \mathrm{IPCE} \times \mathrm{AM\ 1.5} \times 1000/1\mathrm{C} \quad (4)$$

where AM1.5 is the solar photon flux (photons per cm^2), E_{bg} is the material bandgap (~500 nm) and 1C is 6.241×10^{18} electrons per second.

2.4. Computational studies

DFT modelling was undertaken using the CRYSTAL17 program,[58,59] which is based on the expansion of crystalline orbitals through a linear combination of a local basis set consisting of atom centred Gaussian orbitals which are described in previous literature (Bi,[60] V,[61] O[62] and Mo[63]). The PBE0 hybrid functional with 10% HF mixing (PBE0-10) was used to optimise the geometries of Mo doped $BiVO_4$ as it reliably reproduces the structure and electronic properties of complex transition metal oxides.[48,50,51] Geometry optimisation of monoclinic clinobisvanite (m-$BiVO_4$) with space group $I112/b$ (15) and tetragonal scheelite (t-$BiVO_4$) with space group $I4_1/aZ$ (88) was performed from structures found in the literature.[64,65] The optimised $1 \times 1 \times 1$ unit cell of pure m-$BiVO_4$ had the following lattice cell parameters: $a = 5.1217$ Å, $b = 5.1249$ Å, $c = 11.6549$ Å, $\alpha = 89.9985°$, $\beta = 89.9989°$ and $\gamma = 90.6845°$. And the optimised $1 \times 1 \times 1$ unit cell of pure t-$BiVO_4$ had the following lattice cell parameters: $a = 5.1195$ Å, $b = 5.1195$ Å, $c = 11.6278$ Å, $\alpha = 90°$, $\beta = 90°$ and $\gamma = 90°$. $\sqrt{2} \times \sqrt{2} \times 1/\sqrt{2} \times \sqrt{2} \times 2$ supercells of pure m-$BiVO_4$ and t-$BiVO_4$ were constructed using the optimised geometries which contained 8/16 formula units to create Mo substituted structures with 12.5%/6.25% doping at either the V or Bi sites for comparison to the range of Mo doped samples synthesised in this study. The specific V/Bi site to be substituted was found to be inconsequential as the resulting computed ground states were energetically and electronically equivalent.

The exchange and correlation potentials and energy functional were integrated numerically on an atom-centred grid of points. The integration over radial and angular coordinates was performed using Gauss-Legendre and Lebedev schemes, respectively. A pruned grid consisting of 99 radial points and 5 subintervals with (146 302 590, 1 454 590) angular points has been used for all calculations, *i.e.*, the XXLGRID option implemented in CRYSTAL.[58] This grid converges the integrated charge density to an accuracy of about $\times 10^{-6}$ electrons per unit cell. The Coulomb and exchange series are summed directly and truncated using overlap criteria with thresholds of 10^{-7}, 10^{-7}, 10^{-7}, 10^{-7}, and 10^{-14}. Reciprocal space sampling was performed on a Pack–Monkhorst net with a shrinking factor of 4.[58,66,67] The self-consistent field procedure was converged up to a tolerance in the total energy of $\Delta E = 1 \times 10^{-7}$ hartree/primitive unit cell.

Optimised unit cell parameters and atomic coordinates were determined by minimization of the total energy within an iterative procedure based on the total-energy gradient calculated analytically with respect to the cell parameters and nuclear coordinates. Convergence was determined from both the root mean square (rms) and absolute value of the largest component of the forces. The thresholds for the maximum and the rms forces (atomic displacements) were set to 0.00045 and 0.00030 (0.00180 and 0.0012) in atomic units. Geometry optimization was terminated when all four conditions were satisfied simultaneously.

3 Results and discussion

3.1. Synthesis & precursor speciation

Highly phase pure $BiVO_4$ and Mo-doped $BiVO_4$ coatings were grown on FTO glass substrates using a novel AA-CVD method. A range of Mo precursor doping levels from 1 to 12 at% Mo : V were investigated. All coatings were flat and light green in appearance. All coatings passed the Scotch™ tape test,[68] but could be scratched by a diamond tipped pen.

$VO(acac)_2$ was chosen as a low-cost and widely available starting material. This blue compound, dissolves in acetone to give a blue solution, however, the colour rapidly becomes paler and more green upon addition of (wet) MeOH (Fig. 1a). This is due to the rapid reaction with MeOH and water, reported to form $[VO(OH)(Ome)(acac)]^-$, along with release of one H(acac).[69] Under air, this green solution slowly oxidises to generate diamagnetic orange V(v) species which can be studied by ^{51}V NMR spectroscopy (50% oxidation occurs after ~13 h, Fig. 1c). ^{51}V NMR was conducted on a 5 mM solution of $VO(acac)_2$ + $BiPh_3$ in 3 : 1 d_6-acetone/d_4-MeOH, consistent with the precursor solution used for material synthesis, after ageing under air for 30 h. The spectrum (collected over 12 h) revealed three ^{51}V signals at −492 ppm (9%), −502 ppm (30%) and −574 ppm (61%) (Fig. 1b). The major signal at −574 ppm is attributed to $VO(Ome)_3$,[70] without associated acac ligands (N.B. the ^{51}V chemical shift of $VO(Ome)_3$ is reported to be sensitive to concentration and solvent, due to molecular association). The minor signals are attributed to $VO(Ome)(acac)_2$ (−492 ppm) and the dimeric $[VO(Ome)_2(acac)]_2$ (−502 ppm) in which one acac ligand has been lost per V site, based on previously reported analysis.[70] These species, along with the necessarily released acac–H, exist in an equilibrium that is sensitive to solvent and concentration. Under these high-dilution conditions, with MeOH acting as a coordinating solvent, species that have a low acac content are favoured (with free acac–H observed in the associated ^{1}H NMR spectra) (Fig. S2a†). More concentrated solutions of $VO(acac)_2$ in other solvents, $CDCl_3$ (72 mM), C_6D_6 (36 mM) or d_6-acetone (36 mM), with a smaller quantity of MeOH (<10% of solution) resulted in the same three ^{51}V signals

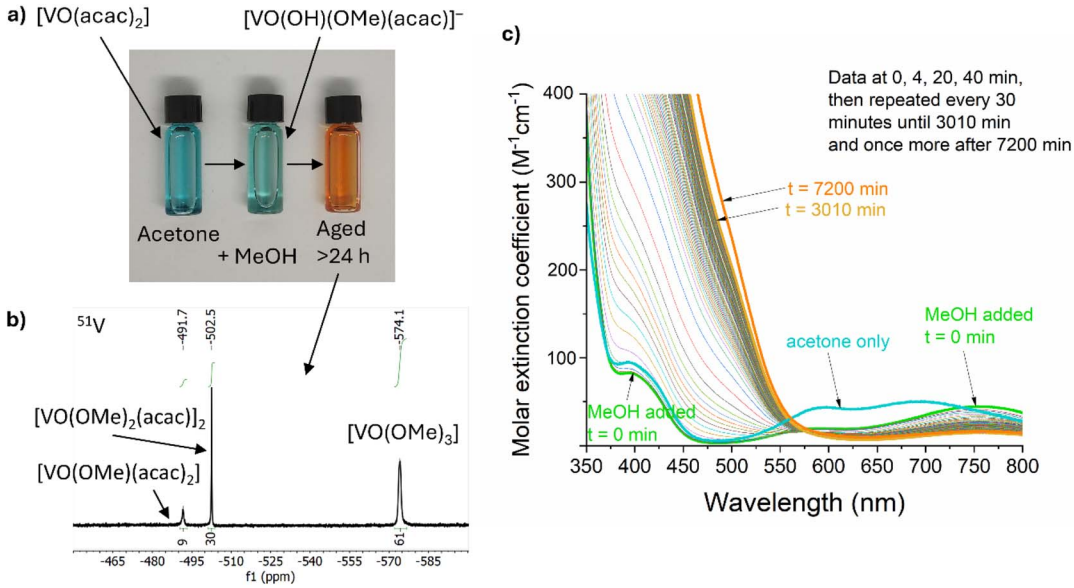

Fig. 1 (a) Photos (left to right) of $VO(acac)_2$ dissolved in acetone, acetone/MeOH, and then after ageing under air. (b) ^{51}V NMR spectrum of a 5 mM solution of $VO(acac)_2$ + $BiPh_3$ in deuterated acetone/MeOH (3 : 1) after oxidation for 30 h under air. (c) Visible absorption spectra of a 5 mM solution of $VO(acac)_2$ in acetone (bold blue line) and 5 mM solution of $VO(acac)_2$ in acetone/MeOH (3 : 1) over time (bold green line, t = 0 min; bold gold line, t = 3010 min; bold orange line, t = 7200 min). $BiPh_3$ was added at the end of the experiment but has no effect on the absorption spectrum.

(with minor chemical shift changes) but with different ratios. These favour acac-rich $VO(Ome)(acac)_2$ as the major component (Fig. S2b†). Recording the spectra at different time points after mixing indicated little change in the equilibrium position, however, at short time periods it is expected that solvolysis of the second acac ligand is much slower than the first.[69] The oxidation of the precursor solution under air (in a sealed cuvette) was monitored over time by visible absorption spectroscopy (Fig. 1c), 50% of the V(IV) signal has been lost after ~13 hours, which is consistent with loss of a broad paramagnetic signal for V(IV) species in the equivalent ^1H NMR data (Fig. S2c†). The oxidation of $VO(acac)_2$ in MeOH has been reported to be first-order with respect to both $[VO(acac)_2(MeOH)]$ and O_2,[69] which was consistent with the conditions studied here, when followed by the loss of the d–d transition absorption signal centred around 750 nm (Fig. 1c and S2d†). The formation of oxidised species causes a change to an orange solution. The kinetics associated with the increase in absorption in the V(v) ligand to metal charge transfer region (<550 nm) are complex, indicating the formation of a shifting equilibrium of species during the transformation (Fig. S2e†). At early time points the LMCT absorptions increase linearly, *e.g.* with ~0^{th} order kinetics, the LMCT band then increases at an elevated rate between 5–7 hours before dropping to a slower rate over prolonged time periods.

Whilst colourless $Mo(CO)_6$ is poorly soluble in acetone/MeOH, slow partial dissolution to give a pale yellow solution occurs over 24 hours. Dissolution is accelerated in the presence of two equiv. acac–H, to give an orange solution. This solution shows a broad ^1H NMR signal at 15.5 ppm, suggesting a paramagnetic Mo compound with organic (acac) ligands. $Mo^{6+}O_2(acac)_2$ is a well-known compound, but would not give a paramagnetic signal, therefore a lower oxidation state of Mo is expected under these conditions. It is possible that reduced Mo compounds form in the precursor solution, especially if acac–H is released during the oxidation of V species. The exact Mo speciation is not easily probed due to the low solubility of $Mo(CO)_6$. Acetone/MeOH solutions of $BiPh_3$ were examined by ^1H NMR spectroscopy, revealing the chemical inertness of $BiPh_3$ under air/moisture and in the presence of $VO(acac)_2$, oxidised V^{5+} species (including excess acac–H) and $Mo(CO)_6$ when studied by ^1H NMR (Fig. S2a†). It appears that $BiPh_3$ remains a well-defined complex under these conditions.

It is clear that the precursor solution is prone to ageing effects over time, driven by the oxidation of V^{4+} by air in the presence of MeOH, which in turn may release acac–H which could, in turn, ligate to oxidised Mo species. Ageing effects are known in the literature in related metal–organic decomposition processes to access $BiVO_4$.[71] Herein, to minimise the effect of ageing in our work, each precursor solution was made fresh for each CVD reaction and used within a period of ~30 min.

3.2. Physical characterisation

3.2.1. XRD and Raman spectroscopy. All coatings were characterised using XRD and Raman spectroscopy (Fig. 2). The XRD pattern of the $BiVO_4$ sample matched that of phase-pure monoclinic clinobisvanite ($I112/b$; a = 5.1903(3) Å, b = 5.0821(3) Å, c = 11.6704(9) Å, $\alpha = \beta = 90°$, γ = 90.28(11)°) (Fig. 2a). This was analogous to previous work by Sagu *et al.* who grew $BiVO_4$ using an alternative AA-CVD route.[14] However, the XRD patterns of all samples doped with Mo differed from $BiVO_4$, with the dual peaks seen at 2θ ~19 and ~29° for $BiVO_4$

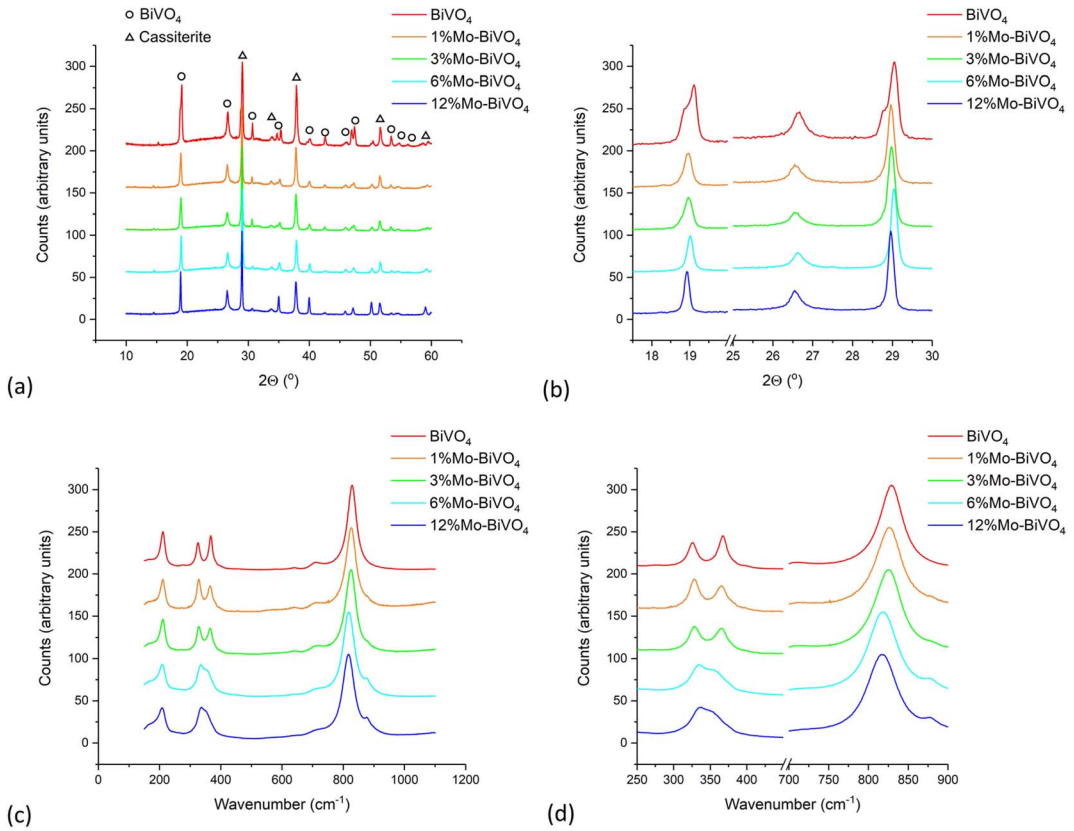

Fig. 2 (a) XRD patterns, (b) close-up view of select peaks in XRD patterns, (c) Raman spectra and (d) close-up view of select peaks in Raman patterns of $BiVO_4$ and all Mo-doped $BiVO_4$ samples.

merging to form single reflections in Mo-doped samples (Fig. 2b). This was attributed to a slight structural distortion, causing the monoclinic lattice to adopt the more symmetric tetragonal form. The XRD patterns of all Mo-doped $BiVO_4$ samples matched that of phase-pure tetragonal scheelite ($I4_1/a$; $a = b = 5.1206(5)$ Å, $c = 5.0821(3)$ Å, $c = 11.5755(10)$ Å, $\alpha = \beta = \gamma = 90°$ for the 1% Mo : $BiVO_4$ sample), with no additional phases observed. In undoped $BiVO_4$, the metastable tetragonal scheelite phase undergoes a phase change to the thermodynamic monoclinic clinobisvanite phase at ~255 °C.[45,72] Herein, the addition of Mo-dopants were found to prevent this phase change, despite the coatings being grown at 400 °C and subsequently annealed in air at 500 °C. This effect was previously observed by Fischer *et al.* in their MOD grown Mo-doped $BiVO_4$ films, where they saw a continuous transition from the monoclinic clinobisvanite to tetragonal scheelite phase with increasing Mo-doping.[37] In their case, the full transition to tetragonal scheelite was observed with ~10.5% Mo-doping. This was also seen by Xiao *et al.* in their electrodeposited Mo-doped $BiVO_4$ films, were full transition to the tetragonal scheelite phase was found with ~10% Mo-doping.[34] Herein, our XRD results indicated a full transition to the tetragonal scheelite phase with only ~2% Mo-doping.

Le Bail models were fit to the XRD patterns, yielding the lattice parameters and average crystal sizes in our coatings. These parameters are plot in Fig. S3† and listed in Table 1. Comparing changes with Mo-doping to an undoped tetragonal scheelite standard ($I4_1/a$; $a = b = 5.105(1)$ Å, $c = 5.0821(3)$ Å, $c = 11.577(1)$ Å, $\alpha = \beta = \gamma = 90°$),[73] we see that the a lattice parameter tended to increase as the Mo-doping level was increased; rising from 5.1903(3) Å in the undoped $BiVO_4$ standard to 5.1349(2) Å in 12% Mo : $BiVO_4$ (Fig. S3a†). However, the reverse trend was seen for the c lattice parameter; decreasing from 11.6705(9) Å in the undoped $BiVO_4$ standard to 11.5592(7) Å in 12% Mo : $BiVO_4$. Overall, there was a general trend for the unit cell volume to increase with Mo-doping; increasing from 301.7(1) $Å^3$ in the undoped $BiVO_4$ standard to 304.8(2) $Å^3$ in 12% Mo : $BiVO_4$. This trend is intuitive, as the Mo^{6+} dopants in a 4-coordinate environment have a higher ionic radius (r ~0.41 Å) than the V^{5+} sites they replace (r ~0.355 Å), causing the unit cell to expand to accommodate them. Correlating with this trend was the increase in average crystal size, increasing from ~25.2 nm in 1% Mo : $BiVO_4$ to ~44.5 nm in 12% Mo : $BiVO_4$.

Raman spectroscopy of the undoped $BiVO_4$ sample corroborated with XRD data, indicating the formation of the monoclinic form (Fig. 2c). The major peaks seen at ~213, ~328, ~368 and ~831 and cm^{-1} corresponded to the external lattice, A_g asymmetric V–O bending, B_g symmetric V–O bending and the A_g symmetric V–O stretching modes, respectively.[74] However, upon doping with increasing levels of Mo, a gradual merging of the A_g asymmetric and B_g symmetric V–O bending modes was observed, whereby at 12% Mo-doping the peaks had almost

Table 1 Summary of the physical properties and PEC performance of $BiVO_4$ and all Mo-doped $BiVO_4$ samples from XRD, XPS, AFM, UV-visible absorption spectroscopy and PEC measurements

		$BiVO_4$	1% Mo–$BiVO_4$	3% Mo–$BiVO_4$	6% Mo–$BiVO_4$	12% Mo–$BiVO_4$
XRD	Crystal type	Clinobisvanite	Scheelite	Scheelite	Scheelite	Scheelite
	Symmetry	Monoclinic	Tetragonal	Tetragonal	Tetragonal	Tetragonal
	a (Å)	5.190(3)	5.120(5)	5.119(5)	5.120(3)	5.134(2)
	c (Å)	11.670(9)	11.575(10)	11.575(10)	11.561(8)	11.559(7)
	γ (°)	90.3(1)	90	90	90	90
	unit cell (Å^3)	307.8(3)	303.5(5)	303.3(5)	303.1(3)	304.7(2)
	Crystal size (nm)	32	25	25	36	45
XPS	Mo : V (%)	—	2.0(1)	4.3(4)	9.6(4)	12.7(14)
AFM	R_q (nm)	22.5	19.7	17.2	27.2	20.7
	Surface area per square micron (μm^2)	1.10	1.13	1.04	1.23	1.08
UV-vis	E_{bg} indirect (eV)	2.55	2.56	2.54	2.54	2.55
	E_{bg} direct (eV)	2.62	2.62	2.61	2.65	2.65
PEC front	[a]400 nm (mA cm^{-2})	0.21	0.41	0.45	0.82	0.60
	TSP (mA cm^{-2})	0.48	0.91	1.02	1.79	1.38
PEC back	[a]400 nm (mA cm^{-2})	0.23	0.25	0.31	0.34	0.23
	TSP (mA cm^{-2})	0.55	0.59	0.74	0.78	0.59

[a] Light power is ~8.5 mW cm^{-2}. Numbers in brackets represent the standard error on the lowest significant figures.

completely merged (Fig. 2d). In addition, we see the introduction of a satellite peak at ~881 cm^{-1}, which increased in intensity with increased Mo-doping, which has previously been assigned to the introduction of a Mo–O–Mo stretching mode.[75] Another effect was the general decrease in energy of all prominent peaks with increased Mo-doping, which is consistent with the elongation of V–O bond length,[75,76] and therefore, an expansion of the unit cell; corroborating with XRD modelling results (Table 1).

3.2.2. XPS analysis. XPS analysis was carried out to identify the chemical nature and composition of our undoped $BiVO_4$ and series of Mo-doped $BiVO_4$ coatings. An example of how the binding energy environments were modelled is shown in Fig. S4† for the 3% Mo–$BiVO_4$ sample. The binding energies and abundances of the chemical states found in the Bi, V, Mo and O binding energy environments are summarised in Table S1† for all samples.

$BiVO_4$ showed the expected peaks in the Bi 4f, V 2p and O 1s binding energy environments. For the Bi 4f environment, Bi $4f_{7/2}$ and Bi $4f_{5/2}$ peaks were seen at ~158.7 and ~164.0 eV, respectively, which have previously been attributed to Bi^{3+} states in $BiVO_4$.[35] No metallic Bi states were observed in the undoped material. For the V 2p environment, V $2p_{3/2}$ and V $2p_{1/2}$ peaks were seen at ~516.1 and ~523.7 eV, respectively, which have previously been attributed to V^{5+} states in $BiVO_4$.[35] A small presence (<4% of the V content) of a reduced V species was observed, with V $2p_{3/2}$ and V $2p_{1/2}$ peaks seen at ~514.7 and ~522.3 eV, respectively, which were attributed to the presence of V^{4+} states.[77] The O 1s environment showed two states; one at ~529.3 eV, which was attributed to metal–oxygen bonds,[78] and another at ~533 eV, which was attributed to carbon–oxygen bonds.[79] The abundance of each element was determined from the peak areas of each environment and corrected using relative sensitivity factors.[80] At the sample surface – as XPS measures ~10 nm deep[81] – the undoped $BiVO_4$ coating was found to be Bi-rich and V-poor. Measurement of the valence band energy region in undoped $BiVO_4$ revealed a valence band maximum, with respect to the Fermi level, of ~1.9 eV (Fig. S5†).

The series of Mo-doped $BiVO_4$ showed broadly similar behaviour to undoped $BiVO_4$, with some notable differences: (i) the binding energy of Bi^{3+} states tended to increase with Mo-doping and (ii) V^{4+} content tended to increase with Mo-doping. As expected, Mo-doped $BiVO_4$ samples showed the presence of Mo species. Across all Mo-doped samples, the average binding energy of the Mo $3d_{5/2}$ state was ~232.3 eV, in agreement with previous studies of Mo-doped $BiVO_4$, and the assignment of a Mo^{6+} environment that substitutes V^{5+} sites.[30–32] Relating this binding energy with previous work on molybdenum oxides, we see that this shows a closer match to Mo_4O_{11} ($Mo^{5.5+}$; 232.1 eV)[82] as compared with MoO_3 (Mo^{6+}; 232.9 eV)[83] and Mo_2O_5 (Mo^{5+}; 231.8 eV).[84] The Mo : V (%) was determined for all samples, and plot in Fig. 3. With increases in Mo precursor doping level, the amount of actual Mo-doping found in the coatings is supra-linear (*i.e.* Mo from the Mo precursor is

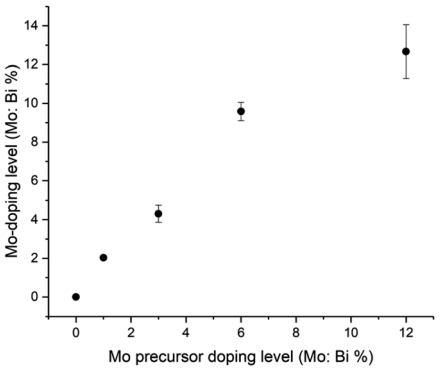

Fig. 3 A plot of the relationship between Mo precursor dopant level (Mo : V %) *vs.* the Mo doping level determined by XPS analysis. All values are the average of 3 unique sample locations; with the error bars representing one standard deviation.

more effective in entering the $BiVO_4$ host lattice than V from the V precursor). However, at higher doping levels (from 6 to 12% Mo precursor doping level) a near linear relationship is seen, which may be due to a nearing of the solubility limit of Mo doping in $BiVO_4$. Importantly, as the Mo-doping level was increased in $BiVO_4$, the valence band maximum (VBM) energy did not significantly change (~1.9 to 2.0 eV; Table S1†). This strongly indicated that Mo doping does not alter the electronic states of the VBM region in $BiVO_4$.

3.2.3. SEM and AFM analysis. Top-down SEM and AFM was carried out on our undoped $BiVO_4$ and series of Mo-doped $BiVO_4$ coatings (Fig. 4). Top-down SEM imaging of our undoped $BiVO_4$ coating revealed densely packed cuboidal particles, that were predominantly ~200 nm wide (Fig. 4a). And top-down SEM imaging of a representative Mo-doped sample (6% Mo : $BiVO_4$) revealed densely packed irregular particles, that were predominantly between ~100 and 150 nm wide (Fig. 4b). XRD modelling showed that average crystal sizes ranged from ~25 to 45 nm in our coatings (Table 1). This indicated the particles seen in SEM were composed from a number of nanocrystals. The coating thickness of a representative 6% Mo : $BiVO_4$ coating was found to be ~180 nm by side-on SEM imaging (Fig. S6†).

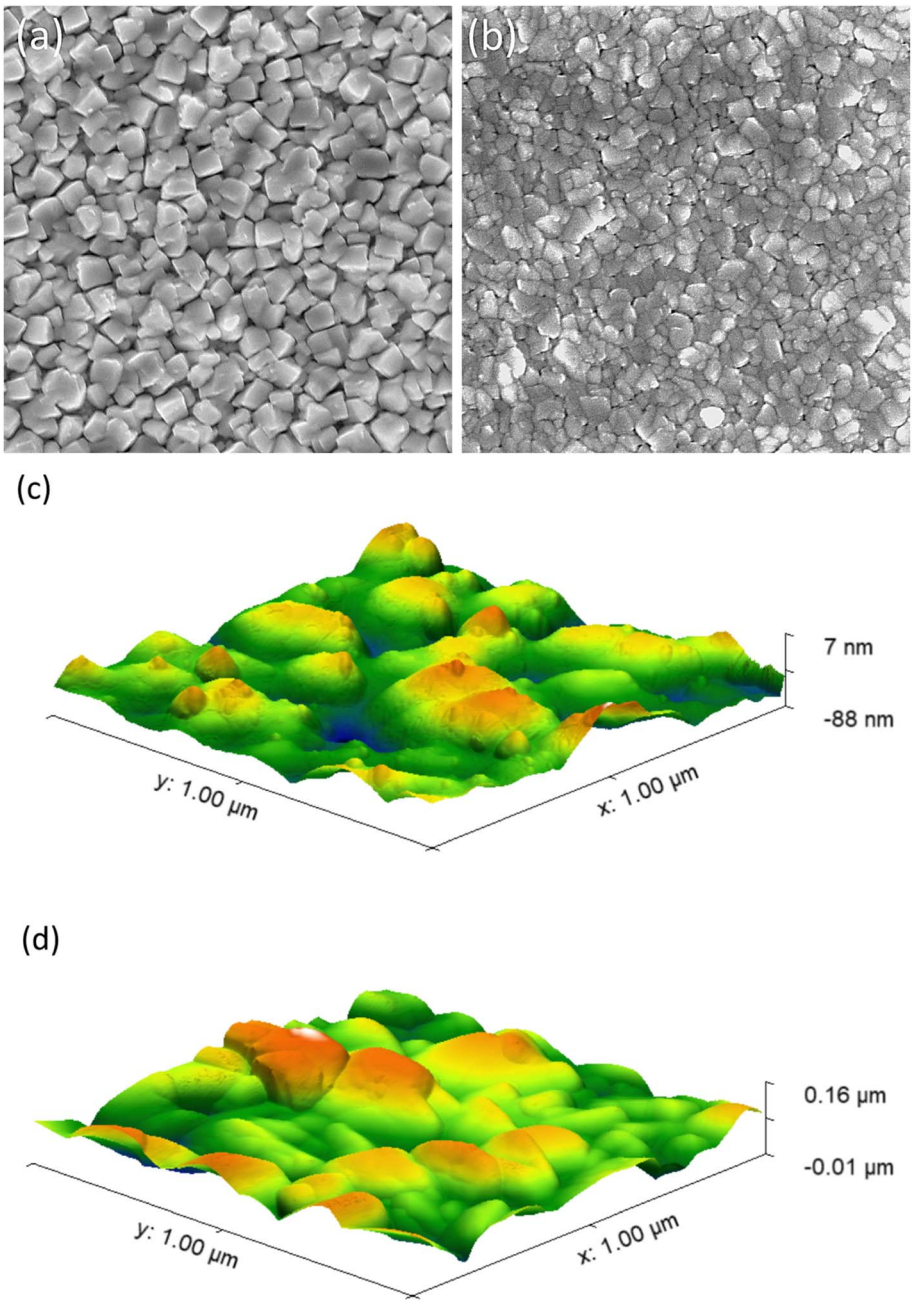

Fig. 4 SEM images of (a) $BiVO_4$ and (b) 6% Mo–$BiVO_4$ taken at 50k magnification [the width of each image represents a distance of 3.8 µm]. AFM images, of (c) $BiVO_4$ and (d) 6% Mo–$BiVO_4$ measured over a 1 µm × 1 µm square area.

Top-down AFM images revealed similar topographies to top-down SEM images for both the undoped $BiVO_4$ (Fig. 4c) and series of Mo-doped $BiVO_4$ coatings (Fig. 4d and S7†). From AFM images, the root mean square roughness (R_q) and surface area per square micron were determined for all samples (Table 1). The R_q ranged from ~17.2 to ~27.2 nm and the surface area per square micron ranged from 1.04 to 1.23 μm^2. No observable trend between the level of Mo-doping and surface roughness or surface area was found. Broadly speaking, all coatings were highly smooth, and showed minimal differences in surface area (up to ~15%).

3.2.4. UV-visible absorption spectroscopy. The UV-visible absorption spectrum was measured for all films (Fig. 5a). All samples, irrespective of their level of Mo-doping, showed broadly similar behaviour. They all showed a band edge at ~480 nm (~2.6 eV) and no additional absorbing states were seen up to 1200 nm. As all samples showed similar coloration by eye, this was to be expected. The indirect allowed and direct allowed transitions were determined through Tauc plots, with a representative example for undoped $BiVO_4$ shown in Fig. S8a.† No significant differences were seen in the range of indirect allowed and direct allowed bandgap energies that were determined (Table 1), with indirect allowed bandgaps ranging between ~2.54 and ~2.56 eV and direct allowed bandgaps ranging between ~2.61 and ~2.65 eV. Notably, in all samples, the indirect allowed transition was consistently lower than the direct allowed transition; in agreement with computational studies.[85] Moreover, the similarity in bandgap energy found between the m-$BiVO_4$ and t-$BiVO_4$ samples was expected, as the monoclinic and tetragonal forms possess similar bandgap energies.[86]

With knowledge of the coating thickness (Fig. S6†), the UV-visible absorption data was used to determine the penetration depth of light (Fig. S8b†).[87] This was used to calculate how different wavelengths of light are absorbed as they travel through our materials, and was done for the cases of UVA (325 nm), violet (400 nm) and blue (475 nm) light for the scenarios of front (Fig. 5b) and back (Fig. 5b) irradiation. Under front irradiation, most UVA (~99%) and violet (~85%) light is absorbed within 100 nm of entering the photoanode. However, only ~43% of blue light is absorbed within 100 nm of entering the photoanode, and only ~64% of blue light is absorbed across the entire 180 nm coating. Under back irradiation, light travels through the FTO layer before reaching the photoanode. Substantial parasitic light absorption is seen in the FTO layer, with this being most significant in the UVA region (~60%

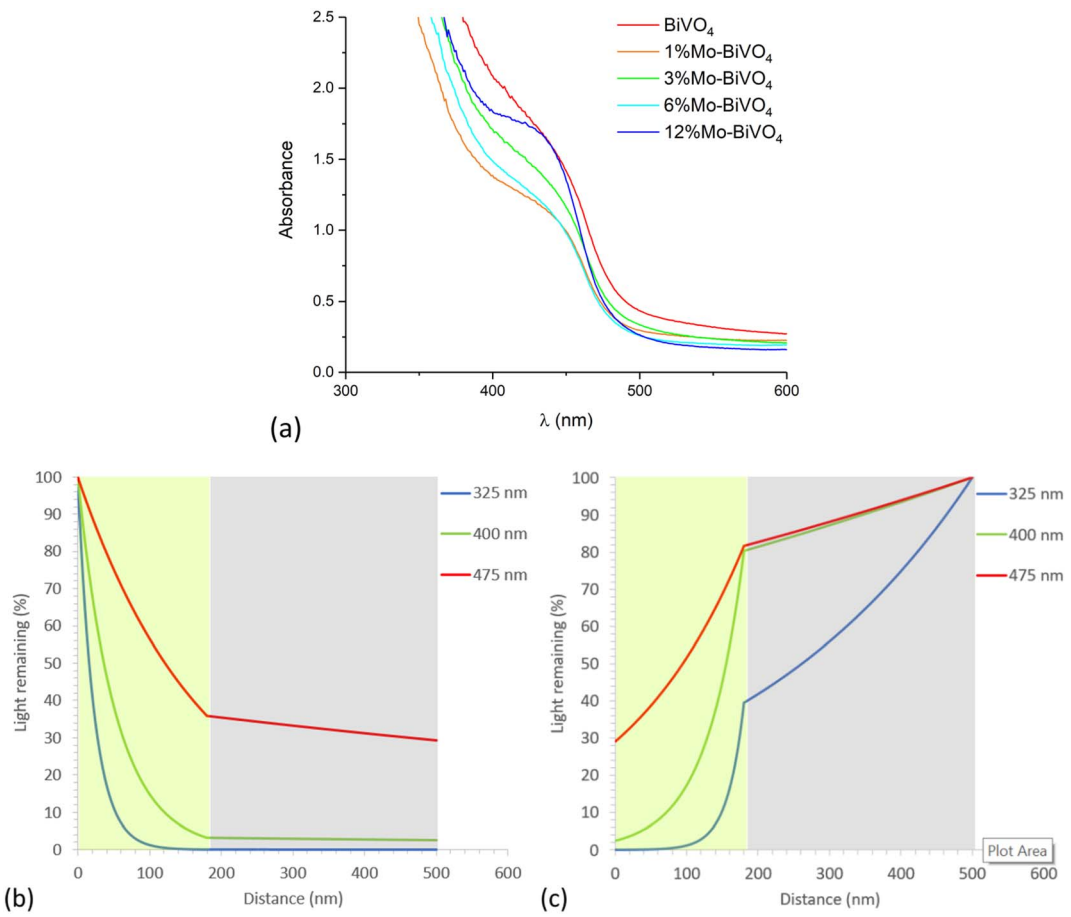

Fig. 5 (a) UV-visible absorption spectra of $BiVO_4$ and all Mo-doped $BiVO_4$ samples and light remaining (%) with distance travelled in 6% Mo–$BiVO_4$ for (b) front irradiation and (c) back irradiation (shaded green and grey areas represent $BiVO_4$ [180 nm thick] and FTO [320 nm thick] layers respectively).

absorbed across the 320 nm FTO coating). The remaining UVA is mostly absorbed (~39%) within the first 100 nm of entering the photoanode. For the cases of violet and blue light, only ~20% of light is parasitically absorbed by the FTO layer. Within 100 nm of entering the photoanode, ~68% and ~35% of the remaining violet and blue light is absorbed, respectively. Under back irradiation, across the entire photoanode, ~39%, ~78% and ~52% of UVA, violet and blue light is absorbed, respectively. Whereas under front irradiation, ~100%, ~97% and ~64% of UVA, violet and blue light is absorbed, respectively.

3.3. Photoelectrochemical water splitting

The PEC water oxidation performance of our undoped $BiVO_4$ and series of Mo-doped $BiVO_4$ was investigated using current–voltage (*JV*) curves in 0.1 M phosphate buffer under 400 nm excitation (Fig. 6). All samples showed similar dark electrocatalytic behaviour, with the onset for water oxidation seen at ~2.0 V_{RHE}. Under illumination, all samples showed a similar onset to photocatalytic water oxidation at ~0.6 V_{RHE}, and did not change for front or back irradiation.

Under front irradiation, the undoped $BiVO_4$ sample showed a slower rise in photocurrent density than the Mo-doped $BiVO_4$ samples, which was indicative of a higher barrier to electron carrier extraction in $BiVO_4$ (Fig. 6a). Although the highest plateau photocurrent density is seen in the 3% Mo : $BiVO_4$ sample, reaching ~1.5 mA cm^{-2} at 2.1 V_{RHE}, the 6% Mo : $BiVO_4$ sample showed the highest photocurrent density at 1.23 V_{RHE} of ~0.82 mA cm^{-2}.

Under back irradiation, all samples showed similar PEC behaviour (Fig. 6b). There was a notable faster rise in photocurrent density in the undoped $BiVO_4$ sample than was seen under front irradiation, which was indicative of a comparatively lower barrier to hole carrier diffusion than electron carrier extraction in the material. Under back irradiation, the 6% Mo : $BiVO_4$ sample showed the highest plateau photocurrent density, reaching ~0.75 mA cm^{-2} at 2.1 V_{RHE}, and highest photocurrent density at 1.23 V_{RHE} of ~0.34 mA cm^{-2}.

Comparing front and back irradiation, the Mo-doped $BiVO_4$ samples showed notably higher photocurrent densities under front irradiation than back irradiation. A plot of the photocurrent density at 1.23 V_{RHE} for front and back irradiation for all samples is shown in Fig. 6c. Similar trends were observed for front and back irradiation, with the photocurrent density consistently rising with increases in Mo precursor doping to 6% Mo : V, before falling at 12% Mo : V. With the exception of the undoped $BiVO_4$ sample, the photocurrent density at 1.23 V_{RHE} was consistently higher for front irradiation than back irradiation. The 6% Mo : $BiVO_4$ sample showed the highest

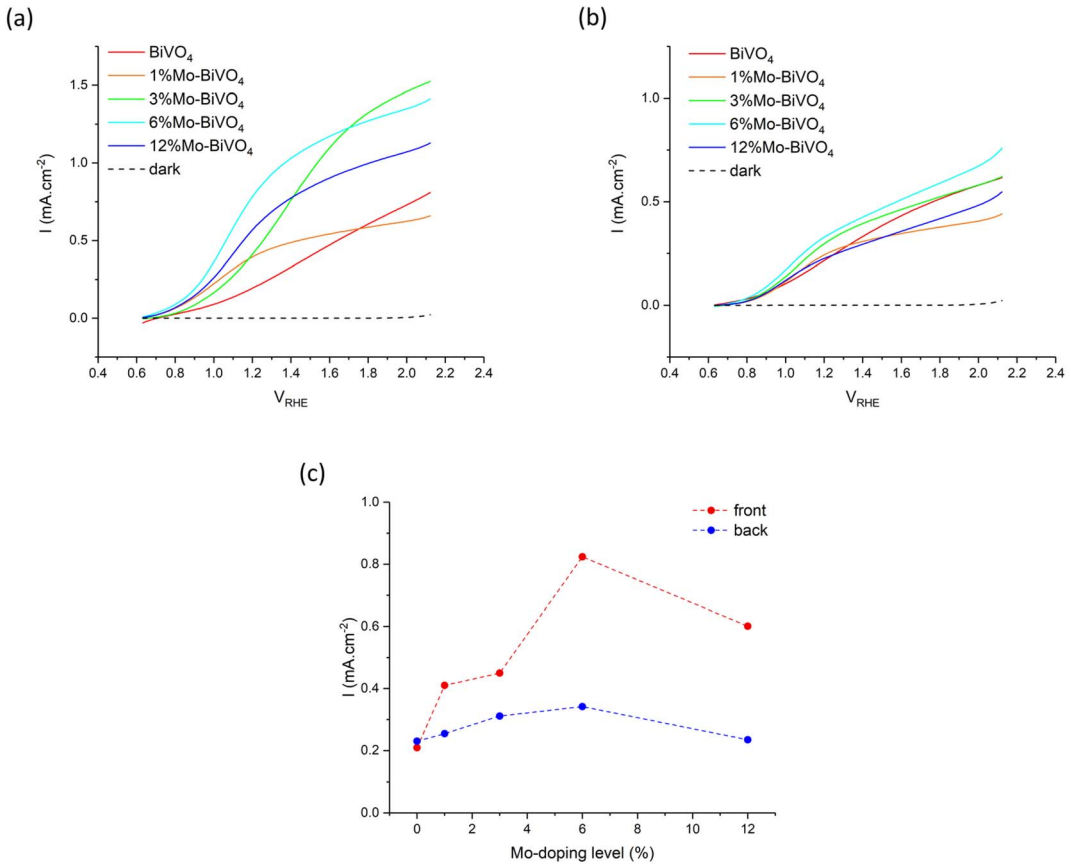

Fig. 6 Current voltage (*JV*) curves for $BiVO_4$ and all Mo-doped $BiVO_4$ samples measured with (a) front irradiation and (b) back irradiation. (c) The photocurrent densities observed at 1.23 V_{RHE} for both front and back irradiation as a function of Mo precursor doping level (%) of $BiVO_4$ and all Mo-doped $BiVO_4$ samples. Samples were measured in 0.1 M phosphate buffer (pH = 7) using 400 nm light (~8.5 mW cm^{-2}).

performance in both cases, reaching photocurrent densities of ~0.82 and ~0.34 mA cm^{-2} for front and back irradiation, respectively. Comparing the photocurrent densities seen at 1.23 V_{RHE}, the performance under front irradiation was up to 2.6 times better than under back irradiation (Table 1). These differences could not be rationalised from the subtle differences in light harvesting of the 400 nm light source, with ~97% absorbed under front irradiation and ~78% absorbed under back irradiation (Fig. 5). Rather, the increases in front irradiation performance, found with Mo-doping, were attributed to enhancements in electron carrier transport and extraction. As back irradiation performance was broadly the same across the series of samples, we conclude that this effect was predominantly limited to improving electron transport (*i.e.* hole carrier transport was largely unaffected by Mo-doping).

The incident photon-to-current efficiency (IPCE) was measured at 1.23 V_{RHE} in 0.1 M phosphate buffer under front and back irradiation for all samples (Fig. 7). Under front irradiation, the undoped $BiVO_4$ sample showed IPCEs of up to ~10% in the ultra-bandgap region. The 6% Mo : $BiVO_4$ sample showed the highest IPCEs, reaching ~50% at 325 nm. Similar to *JV* curve measurements, the IPCE performance consistently increased with Mo-doping from 0 to 6% Mo : V, and then decreased at 12% Mo : V. Under back irradiation, IPCEs were significantly lower than those measured under front irradiation. This, in part, was due to the parasitic absorption of light by the FTO substrate, which absorbed most strongly in the UV region. However, IPCEs in the visible region where the parasitic absorption of light was limited (to ~20%) were substantially lower than those measured under front irradiation. Under back irradiation, the 6% Mo : $BiVO_4$ sample showed the highest IPCEs, reaching ~14% at 400 nm. This was less than half the value observed under front irradiation (~30% at 400 nm). Importantly, under back irradiation, Mo-doping granted only marginal increases in performance compared with undoped $BiVO_4$, which is in line with the accepted hypothesis that Mo-doping primarily improves the conductivity of photogenerated electron carriers.

Under front irradiation, the highest IPCEs were seen in the UV region, where light is absorbed most prominently near the surface of the material (~75% of 325 nm light absorbed within 30 nm of entering the material). Under front irradiation, the 6% Mo : $BiVO_4$ sample showed IPCEs in the ultra-bandgap region between 4 and 5 times higher than undoped $BiVO_4$, whereas under back irradiation, the 6% Mo : $BiVO_4$ sample showed IPCEs in the ultra-bandgap region between 1 and 1.5 times higher than undoped $BiVO_4$. As the optical properties of both materials were similar, overall, these trends indicated that electron carrier transport and extraction was enhanced by a factor of between 4 and 5 with Mo doping, and that hole carrier transport was largely unaffected.

The theoretical solar photocurrent (TSP) was determined by multiplying the IPCE measured at 1.23 V_{RHE} with the solar spectrum (AM1.5) and integrating the photon-to-current flux (eqn (4); Fig. 8). Undoped $BiVO_4$ showed TSPs of ~0.48 and ~0.55 mA cm^{-2} for front and back irradiation, respectively. In all cases, Mo-doping increased the TSP, with 6% Mo : $BiVO_4$ showing the highest TSPs of ~1.79 and ~0.78 mA cm^{-2} for front and back irradiation, respectively. Similar to *JV* and IPCE curves, TSPs were significantly higher (up to a factor of ~2.3) for front irradiation than back irradiation. This, as mentioned above, is attributed to the improvement in electron carrier transport and extraction with Mo-doping.

The photoelectrochemical water oxidation performance of the samples produced herein is now compared with the literature; summarised in Table 2. Herein, we compare $BiVO_4$ produced by CVD routes (akin to this work) and Mo-doped $BiVO_4$ produced by any synthetic route. It should be noted, for fair comparisons to be made, more complex $BiVO_4$-based structures are not included in this table (*e.g.* surface modified $BiVO_4$ with a co-catalyst to improve surface reaction kinetics, or the formation of a $BiVO_4$-based heterojunction to improve charge carrier separation, *etc.*).

Sagu *et al.* used an AA-CVD method to produce m-$BiVO_4$ photoanodes.[14,15] Porous irregular particles (~500 nm wide) of $BiVO_4$ were formed when ethylene glycol was used to dissolve their bismuth precursor, which when examined in 0.5 M $Na_2SO_{4(aq.)}$, showed an onset potential of ~1.0 V_{RHE} and a photocurrent density of ~0.15 mA cm^{-2} at 1.23 V_{RHE} and 1 sun irradiance.[15] Smaller porous irregular particles (~75 nm wide)

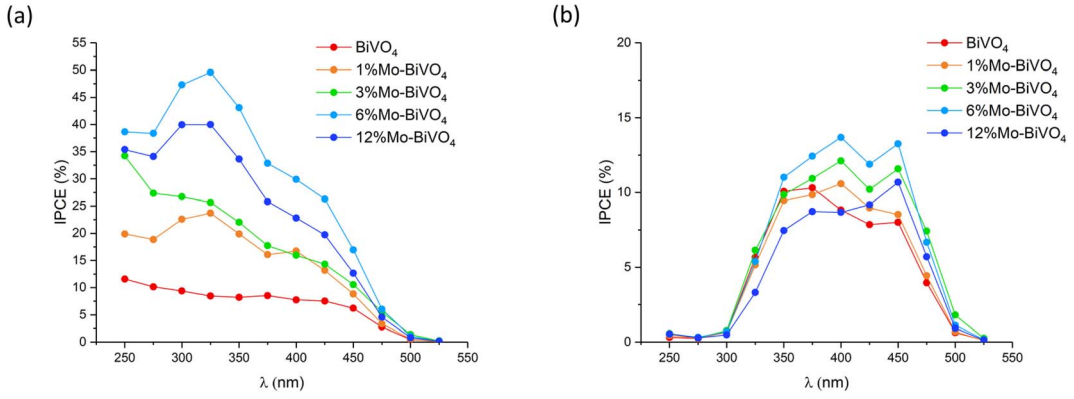

Fig. 7 Incident photon to current efficiency (IPCE) curves for $BiVO_4$ and all Mo-doped $BiVO_4$ samples measured with (a) front irradiation and (b) back irradiation. Samples were measured in 0.1 M phosphate buffer (pH = 7) at 1.23 V_{RHE}.

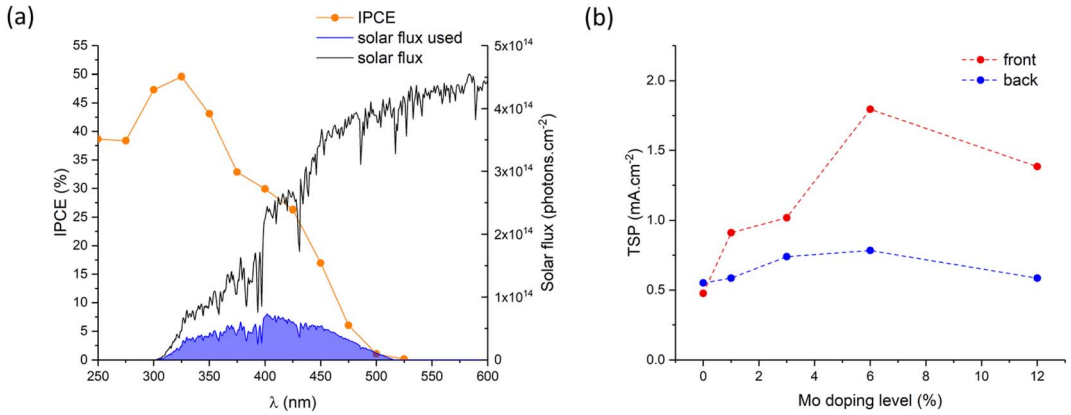

Fig. 8 (a) Calculation of the theoretical solar photocurrent (TSP) for 6% Mo–$BiVO_4$ under front irradiation at 1.23 V_{RHE} and (b) a summary of the TSP photocurrents at 1.23 V_{RHE} for front and back irradiation as a function of Mo precursor doping level (%) of $BiVO_4$ and all Mo-doped $BiVO_4$ samples.

of $BiVO_4$ were formed when acetylacetone was used to dissolve their bismuth precursor, which when examined in 1 M $Na_2SO_{4(aq.)}$, showed an onset potential of ~0.6 V_{RHE} and a photocurrent density of ~0.40 mA cm^{-2} at 1.23 V_{RHE} and 1 sun irradiance.[14] Gupta *et al.* used a DLI-CVD method to produce m-$BiVO_4$ photoanodes.[17] Densely packed rounded particles (~0.2 to 1 μm wide) of $BiVO_4$ were formed, which when examined in 0.5 M $KOH_{(aq.)}$, showed an onset potential of ~0.23 V_{RHE} and a photocurrent density of ~2.10 mA cm^{-2} at 1.23 V_{RHE} and 1 sun irradiance (although it should be noted that the photocurrent density decreased rapidly in this high pH electrolyte). Ager *et al.* used a VT-CVD method to produce m-$BiVO_4$ photoanodes.[16]

Table 2 Summary of the synthetic routes, doping level, material structure and photoelectrochemical water oxidation performance for $BiVO_4$ produced by CVD methods and Mo-doped $BiVO_4$ photoanodes produced by any method

Photoanode	Synthesis method	[a]Mo : V doping level (%)	Material structure	[b]J_{on} (V_{RHE})	[c]J (mA cm^{-2})	Reference
$BiVO_4$	AA-CVD	na	Porous irregular particles (~500 nm wide)	~1.0	~0.15	Sagu *et al.*[15]
		na	Porous irregular particles (~75 nm wide)	~0.6	~0.40	Sagu *et al.*[14]
	DLI-CVD	na	Densely packed rounded particles (~0.2 to 1 μm wide)	~0.23	~2.10	Gupta *et al.*[17]
	VT-CVD	na	Densely packed rounded particles (~200 nm)	~0.3[d]	~0.95[d]	Ager *et al.*[16]
	AA-CVD	na	Densely packed cuboidal particles (~200 nm wide)	~0.6	~0.55	herein
Mo–$BiVO_4$	Electro-deposition	1.25 (1.8)	Open nanoporous structure	~0.5	~0.85	Choi *et al.*[88]
		ns (ns)	Wormlike nanostructure (~100 nm wide)	~0.4	~1.4	Ao *et al.*[35]
		3 (3)	Wormlike nanostructure (~100 nm wide)	~0.55	~1.9	Xiao *et al.*[34]
	Electro-spinning	ns (ns)	1D nanofibres	~0.7	~0.15	Hwang *et al.*[31]
		2.0 (3.0)	Irregular mesoporous network	~0.5	~0.77	Wong *et al.*[30]
	ESD	0.15 (ns)	Nanotextured pillars (~10 μm tall)	~0.7	~0.7	Yoon *et al.*[32]
	MOD	2.0 (4.5)	Mesoporous structure	~0.4	~0.4	Herring *et al.*[41]
		0.5 (ns)	Dense, irregularly particles (~50 nm wide)	ns	~1.1[d,f]	Kudo *et al.*[38]
		10 (6)	Dense, wormlike particles (~50 nm wide)	~0.5	~1.9	Fischer *et al.*[37]
		ns (3.0)	Nanoporous (~100 nm wide particles)	~0.4	~2.1	Cui *et al.*[39]
		3.0 (6.5)	Compact nanoporous structure (~150 nm wide particles)	~0.4	~2.2[e]	Zou *et al.*[40]
	PVD	1.0 (1.0)	Nanostructured wormlike arrays (~100 nm in diameter)	~0.3[d]	~2.1[d]	Zhang *et al.*[43]
		ns (3.0)	Porous irregular particles (~200–400 nm wide)	~0.3[d]	~3.5[d]	Ager *et al.*[42]
	AA-CVD	6.0 (9.6)	Densely packed irregular particles (~100 to 150 nm wide)	~0.6	~1.79	herein

[a] Represents the amount added during synthesis, and in brackets, represents the amount measured by an analytical technique. [b] The photocurrent onset potential. [c] Photocurrent observed at 1.23 V_{RHE} using a simulated solar light source of 1 sun power (100 mW cm^{-2}) or TSP derived from IPCE measurements. na = not applicable; ns = not stated. [d] Examined in a hole scavenger solution. [e] Lamp power not stated. [f] Measured at ~1.13 V_{RHE}.

Densely packed rounded particles (~200 nm) of $BiVO_4$ were formed, which when examined in a hole scavenger solution of 0.5 M $Na_2SO_{3(aq.)}$, showed an onset potential of ~0.3 V_{RHE} and a photocurrent density of ~0.95 mA cm^{-2} at 1.23 V_{RHE} and 1 sun irradiance. Herein, an AA-CVD method was used to produce m-$BiVO_4$ photoanodes. Films with densely packed cuboidal particles (~200 nm wide) of $BiVO_4$ were formed, which when examined in 0.1 M phosphate buffer, showed an onset potential of ~0.6 V_{RHE} and a TSP of ~0.55 mA cm^{-2} when irradiated from the back. The PEC performance of the $BiVO_4$ photoanodes grown herein, using AA-CVD, compared favourably with previous work where alternative CVD routes were also used; displaying median onset potentials and photocurrent densities (Table 2).

Mo-doped $BiVO_4$ has been synthesised using a range of methods.[30–32,34–43] Choi *et al.* used an electrodeposition method to produce Mo-doped $BiVO_4$ with open nanoporous structures.[88] They studied range of precursor doping levels from 0.5 to 3%, and found that the most photoelectrochemically active sample contained 1.8% Mo : V. They studied the activity of this sample in 1 M NaH_2PO_4 buffer, which showed an onset potential of ~0.5 V_{RHE} and a photocurrent density of ~0.85 mA cm^{-2} at 1.23 V_{RHE} and 1 sun irradiance. Ao *et al.* also used an electrodeposition method to produce Mo-doped $BiVO_4$.[35] The films possessed worm-like nanostructure (~100 nm wide). Their samples were tested in 0.1 M $Na_2SO_{4(aq.)}$, with the most active sample showing an onset potential of ~0.4 V_{RHE} and a photocurrent density of ~1.4 mA cm^{-2} at 1.23 V_{RHE} and 1 sun irradiance. To our knowledge, the Mo-doping level was not stated for these samples (despite XPS analysis being carried out). And Xiao *et al.* produced Mo-doped $BiVO_4$ by electrodeposition.[34] Similar to Ao *et al.*,[35] worm-like nanostructures were formed. A range of doping concentrations were examined (from ~1 to ~10%), with the most active sample containing ~3% Mo : V. In 0.5 M phosphate buffer, the best performing sample showed an onset potential of ~0.55 V_{RHE} and a photocurrent density of ~1.9 mA cm^{-2} at 1.23 V_{RHE} and 1 sun irradiance.

Hwang *et al.* grew Mo-doped $BiVO_4$ using an electrospinning method, producing 1D nanofibers.[31] The best performing sample, when examined in 0.1 M phosphate buffer, showed an onset potential of ~0.7 V_{RHE} and a photocurrent density of ~0.15 mA cm^{-2} at 1.23 V_{RHE} and 1 sun irradiance. The Mo-doping level added or achieved was not stated. Wong *et al.* also used electrospinning route, producing Mo-doped $BiVO_4$ films formed from irregular mesoporous networks.[30] Their best performing sample contained 3% Mo : V, and when examined in 0.5 M $Na_2SO_{4(aq.)}$, showed an onset potential of ~0.5 V_{RHE} and a photocurrent density of ~0.77 mA cm^{-2} at 1.23 V_{RHE} and 1 sun irradiance.

Yoon *et al.* grew Mo-doped $BiVO_4$ using an ESD method, forming nanotextured pillars that were ~10 μm tall.[32] They studied a range of Mo-doping levels from 0.05 to 0.20%, and found that the highest performance was seen in films with a 0.15% precursor doping level. The photoelectrochemical activity was investigated in 1 M Na_2SO_4, showing an onset potential of ~0.7 V_{RHE} and a photocurrent density of ~0.7 mA cm^{-2} at 1.23 V_{RHE} and 1 sun irradiance.

Using a surfactant-assisted MOD route, Herring *et al.* produced mesoporous Mo-doped $BiVO_4$ films.[41] Their optimal sample was produced from a 2.0% Mo : V precursor ratio, producing a film with 4.5% Mo : V doping. This was examined in 0.5 M $Na_2SO_{4(aq.)}$ phosphate buffer, and showed an onset potential of ~0.4 V_{RHE} and a photocurrent density of ~0.4 mA cm^{-2} at 1.23 V_{RHE} and 1 sun irradiance. Kudo *et al.* produced densely packed, irregularly shaped particles (~50 nm wide) using MOD.[38] A range of Mo precursor doping levels were studied (from 0.25 to 1.5%). The optimum Mo precursor doping level was found to be 0.5%; however, the doping level achieved in the sample was not stated. The photoanode was studied in 0.1 M $K_2SO_{4(aq.)}$ in the presence of a hole scavenger 0.01 M $K_2SO_{3(aq.)}$, and achieved a photocurrent density of ~1.1 mA cm^{-2} at ~1.13 V_{RHE} at 1 sun irradiance. Fischer *et al.* also used MOD to synthesise Mo-doped $BiVO_4$.[37] Their coatings were made of dense, wormlike particles (~50 nm wide). A wide range of Mo precursor doping levels were studied (0 to 20%). The sample containing 6% Mo : Bi doping showed the highest photoelectrochemical performance, where when examined in 0.1 M potassium phosphate buffer, showed an onset potential of ~0.5 V_{RHE} and a photocurrent density of ~1.9 mA cm^{-2} at 1.23 V_{RHE} and 1 sun irradiance. Nanoporous (~100 nm wide particles) Mo-doped $BiVO_4$ was produced using MOD by Cui *et al.*[39] Their best performing sample contained a 3% Mo : V doping level, and when examined in 0.5 M KH_2PO_4 buffer, showed an onset potential of ~0.4 V_{RHE} and a photocurrent density of ~2.1 mA cm^{-2} at 1.23 V_{RHE} and 1 sun irradiance. And Zou *et al.* used MOD to synthesise compact nanoporous films of Mo-doped $BiVO_4$.[40] Their most active sample was contained 6.5% Mo : V, which when examined in 0.5 M $Na_2SO_{4(aq.)}$, showed an onset potential of ~0.4 V_{RHE} and a photocurrent density of ~2.2 mA cm^{-2} at 1.23 V_{RHE} (Xe lamp; irradiance power not stated).

Zhang *et al.* grew Mo-doped $BiVO_4$ using a pulsed laser PVD route.[43] Nanostructured wormlike structures were formed, which were ~100 nm in diameter. A range of Mo-doping levels were studied (from 0.5 to 5.0%), where it was found that 1.0% Mo : V doping resulted in the highest performing photoanodes. When examined in a 0.1 M phosphate buffer solution with a 0.1 M $Na_2SO_{3(aq.)}$ hole scavenger, the optimal sample showed an onset potential of ~0.3 V_{RHE} and a photocurrent density of ~2.1 mA cm^{-2} at 1.23 V_{RHE} and 1 sun irradiance. Ager *et al.* grew Mo-doped $BiVO_4$ using a reactive co-sputtering PVD method, forming porous irregular particles (~200–400 nm wide).[42] A range of Mo-doping levels were studied (from 1.0 to 5.5%). It was found that 3% Mo : V doping resulted in the highest performing films. The photoelectrochemical performance was examined in 1 M phosphate buffer with 0.1 M $Na_2SO_{3(aq.)}$ hole scavenger, showing an onset potential of ~0.3 V_{RHE} and a photocurrent density of ~3.5 mA cm^{-2} at 1.23 V_{RHE} and 1 sun irradiance.

Herein, an AA-CVD method was used to produce Mo-doped t-$BiVO_4$ photoanodes, forming densely packed irregular particles (~100 to 150 nm wide). A range of Mo-doping levels were investigated (from ~2.0 to ~12.7% doping level achieved), where the highest performance was observed (for both front

and back irradiation) was a 9.6% Mo-doped sample. This sample, when examined in 0.1 M phosphate buffer, showed an onset potential of ~0.6 V_{RHE} and a TSP of ~1.79 mA cm^{-2} when irradiated from the front. Despite there being a wide range of Mo-doping levels studied to date, there is no consensus on what the optimum Mo-doping level; ranging from ~1.0 to 9.6% Mo : V%. This we attribute to the range of methods used to produce Mo-doped $BiVO_4$, resulting in a wide range of topographies, average crystal sizes and defect densities. However, what can be said is that the photoelectrochemical performance of the best performing Mo-doped $BiVO_4$ photoanode produced herein using AA-CVD showed photocurrent densities (TSP up to 1.79 mA cm^{-2}) at the higher end of what has previously been achieved for this material (up to 2.1 mA cm^{-2} at 1.23 V_{RHE} and 1 sun irradiance[42]) (Table 2).

3.4. Computational studies

Hybrid exchange DFT calculations studies were carried out on the $BiVO_4$ system to determine the effect of Mo doping substituting for Bi or V sites, at 6.25 or 12.5 at%, with respect to the metal being replaced, in both the m-$BiVO_4$ and t-$BiVO_4$ host structures. Herein we describe the effect of Mo doping on the thermodynamically most stable structure computed and report computed PDOS and the spin density.

3.4.1. Structure. The structures of undoped t-$BiVO_4$ and m-$BiVO_4$ are shown in Fig. S9,† and their lattice parameters are shown in Tables 3 and 4, respectively. For t-$BiVO_4$, the calculated unit cell parameters in the *a*, *b* and *c* directions were marginally higher than those deduced from room temperature XRD, and resulted in a comparatively expanded unit cell volume (~1.0% expansion *vs.* experimental observations). Conversely, for m-$BiVO_4$, the calculated unit cell parameters in the *a* and *b* directions were marginally lower than XRD measurements, and resulted in a comparatively contracted unit cell volume (~1.4% contraction *vs.* experimental observations). Overall, these differences are small and typical of fully converged hybrid exchange DFT calculations for strongly correlated systems.

Experimental studies conducted herein showed that our 6% Mo–$BiVO_4$ sample produced the most active photoanode for water splitting under both front and back irradiation (Fig. 8b), which XPS, XRD and Raman spectroscopy analysis showed contained a Mo doping level of ~9.6 at% in V sites in a t-$BiVO_4$ structure. The calculated analogous t-$BiVO_4$ structure, at a similar level of Mo doping (6.25 at% in V sites) is shown in Fig. 9. A comparison of the unit cell lattice parameters shows that Mo doping in V sites results in an expansion in the unit cell volume of ~0.79% compared to the undoped structure, with the biggest change in lattice parameter seen in the *a* direction (~0.48% increase). A similar level of unit cell expansion of ~0.46% was seen experimentally in the 6% Mo–$BiVO_4$ sample (Table 1). Our calculations showed that a higher level of Mo doping of 12.5 at% in V sites resulted in a further increase in the unit cell expansion of ~1.72% compared to the undoped structure.

In both t-$BiVO_4$ and m-$BiVO_4$, V^{5+} ions are coordinated by four O atoms in tetrahedral sites and Bi^{5+} ions are coordinated by eight oxygen atoms in cubic hole sites. Comparing the Shannon crystal radii for Mo replacing such sites, one would expect an expansion in the unit cell with Mo replacing V sites and a contraction with Mo replacing Bi sites.[89] In the undoped t-$BiVO_4$ structure, the average calculated V–O bond distance in the VO_4 tetrahedral units is 1.734 Å. Where the Mo dopant replaced V, the resulting MoO_4 tetrahedral unit formed had an average Mo–O bond distance of 1.839 Å. This indicated that doped Mo ions have an effective radius of ~0.11 Å larger than vanadium; this corresponds well with the Shannon ionic radii, where V and Mo ions in the 5+ state in a 4-coordinate environment show crystal radii of 0.495 Å and 0.60 Å, respectively.[89]

As detailed above, Mo dopants at V sites retain a single electron in a 4d derived orbital, which acts as a n-dopant and is likely to contribute to increased conductivity. The computed spin density at a Mo doping of 6.25 at% at a V site in t-$BiVO_4$ is shown in Fig. 11b. It is clear that at this level of doping, the electron remains mostly localised to the local 4d orbital of Mo, with only some donation seen with neighbouring O ions in the MoO_4 unit, and a small donation seen to nearby V ions.

The calculated structures for m-$BiVO_4$ with 6.25 at% Mo doping of a V site is shown in Fig. S10,† t-$BiVO_4$ and m-$BiVO_4$ with 6.25 at% Mo doping of a Bi site are shown in Fig. S11 and S12,† respectively, t-$BiVO_4$ and m-$BiVO_4$ with 12.5 at% Mo doping of a V site are shown in Fig. 10 and S13,† respectively, and t-$BiVO_4$ and m-$BiVO_4$ with 12.5 at% Mo doping of a Bi site are shown in Fig. S14 and S15,† respectively. The lattice

Table 3 Table listing and comparing the calculated lattice parameters (*a*, *b*, *c*, *α*, *β*, *γ*), unit cell volumes (Å^3) and change in unit cell volume *vs.* the undoped structure for the undoped and Mo-doped t-$BiVO_4$ structures studied herein

Mo-doped t-$BiVO_4$					
Dopant site	n/a	V		Bi	
Doping level (at%)	0	6.25	12.5	6.25	12.5
a (Å)	5.1195	5.1442	5.1522	5.1091	5.0919
b (Å)	5.1195	5.1307	5.1522	5.1093	5.0916
c (Å)	11.6278	11.6387	11.6785	11.6409	11.6409
α (°)	90	90	90	89.5445	90.1624
β (°)	90	90	90	90.0542	90.6944
γ (°)	90	90.7870	90	89.6033	90.2061
Vol. (Å^3)	304.756	307.154	310.011	303.858	301.771
Vol. change *vs.* undoped (%)	n/a	0.79	1.72	−0.29	−0.98

Table 4 Table listing and comparing the calculated lattice parameters (a, b, c, α, β, γ), unit cell volumes (Å^3) and change in unit cell volume *vs.* the undoped structure for the undoped and Mo-doped m-$BiVO_4$ structures studied herein

Mo-doped m-$BiVO_4$					
Dopant site	n/a	V		Bi	
Doping level (at%)	0	6.25	12.5	6.25	12.5
a (Å)	5.1217	5.1299	5.1293	5.1090	5.0929
b (Å)	5.1249	5.1447	5.1749	5.1093	5.0929
c (Å)	11.6549	11.6360	11.6208	11.6407	11.6419
α (°)	89.9985	90.0004	90.0032	90.4560	90.7593
β (°)	89.9989	89.9930	90.0022	90.0549	90.1496
γ (°)	90.6845	90.7784	91.1004	90.3914	90.2804
Vol. (Å^3)	305.899	307.070	308.402	303.848	301.928
Vol. change *vs.* undoped (%)	n/a	0.38	0.82	−0.67	−1.30

parameters for these Mo doped t-$BiVO_4$ and m-$BiVO_4$ structures are shown in Tables 3 and 4, respectively.

As expected from the localised nature of the doped electron and the effect of ionic radius on the local tetrahedral environment the overall effect on the lattice is homogeneous in the level of doping. Relatively consistent changes in the unit cell lattice parameters were seen with Mo doping in V and Bi sites for the t-$BiVO_4$ and m-$BiVO_4$ host structures, with expansions/contractions in volume seen with Mo doping of V/Bi sites (Fig. S16a†). This was also consistent with what was seen in our experiments, where Mo doping of V sites in a t-$BiVO_4$ structure resulted in an expansion of the unit cell volume (Fig. S16b†), and therefore, validated our calculations. Regarding average metal oxygen bond lengths in both m-$BiVO_4$ and t-$BiVO_4$ structures, for the case of Mo dopants replacing V sites (*i.e.* tetrahedral hole sites with 4-coordinating O ions), the average bond length increased by ~0.1 Å, and for the case of Mo dopants replacing Bi sites (*i.e.* cubic hole sites with 8-coordinating O ions), the average bond length decreased by ~0.35 Å, which are both in agreement with the expected outcomes from Shannon crystal radii.[89]

The total energy of each calculated structure was compared (values are per unit of the largest doped supercell – 16 formula units). In line with our experiments, it was energetically more favourable, by ~2.37 meV per cell, for undoped m-$BiVO_4$ to form compared with undoped t-$BiVO_4$. Again, in line with our experiments, this changed with Mo doping at 6.25 at% in V sites, with t-$BiVO_4$ becoming more favourable by ~2.33 meV per cell. At 12.5 at% Mo doping in V sites, the difference was negligible, with m-$BiVO_4$ being more favourable by only ~0.13 meV. Regarding Mo doping Bi sites, the difference was negligible at 6.25 at% doping, with t-$BiVO_4$ being more favourable by only ~0.19 meV, and more significant at 12.5 at% doping, with m-$BiVO_4$ being more favourable by ~3.05 meV. These are relatively small energetic differences and thermal fluctuations at

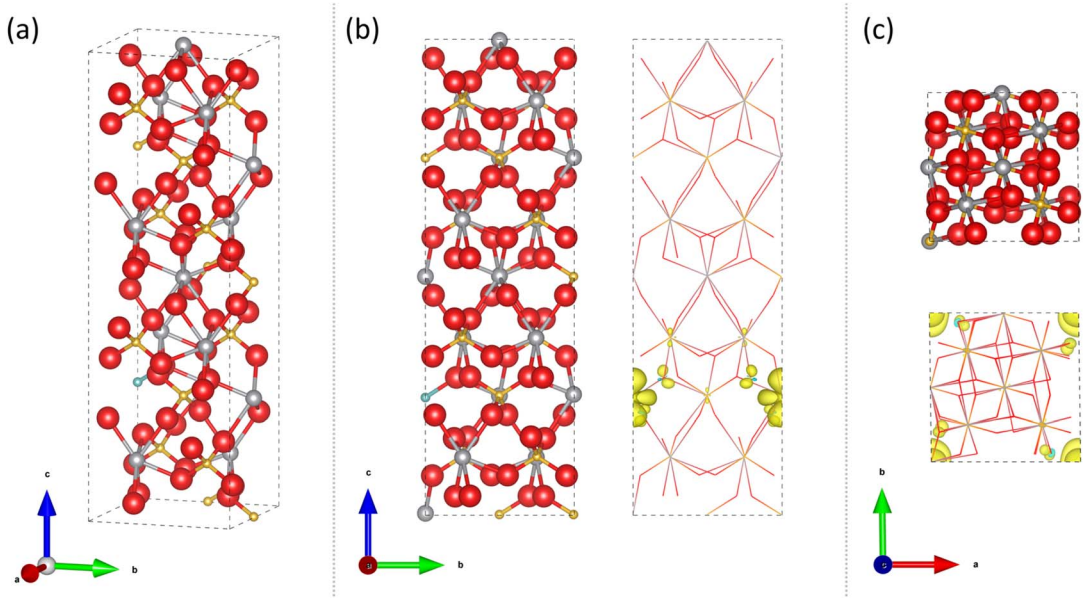

Fig. 9 Calculated structure for 6.25 at% Mo doping of a V site in t-$BiVO_4$ for a 2 × 1 × 1 supercell showing atomic positions and spin density [Bi = silver, V = gold, O = red, Mo = light blue; ionic radii proportions scaled down for visibility]. (a) Angled view, (b) a-axis view and (c) c-axis view.

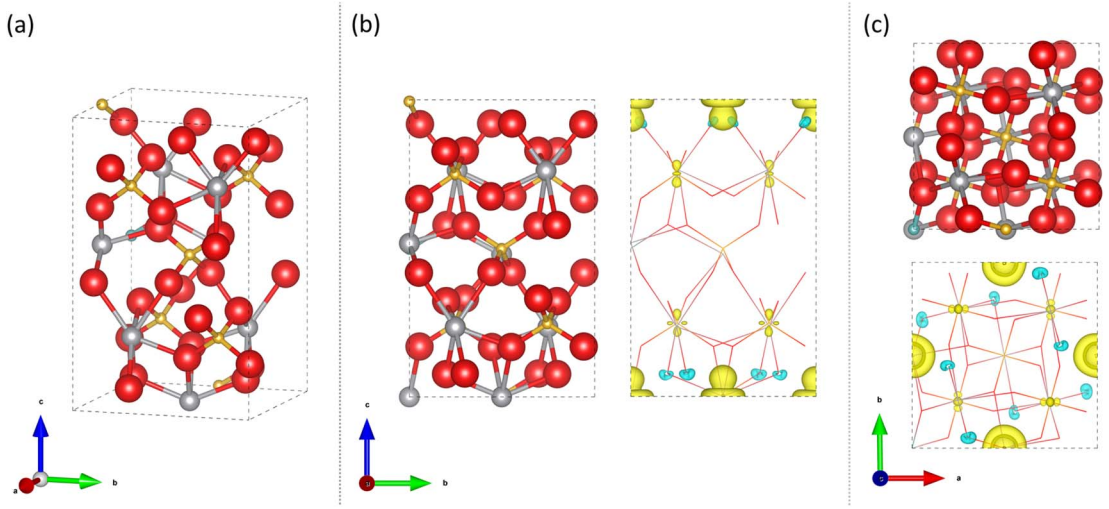

Fig. 10 Calculated structure for 12.5 at% Mo doping of a V site in tetragonal scheelite $BiVO_4$ for a single unit cell showing atomic positions and spin density [Bi = silver, V = gold, O = red, Mo = light blue; ionic radii proportions scaled down for visibility]. (a) Angled view, (b) *a*-axis view and (c) *c*-axis view.

room temperature would be expected to produce a somewhat disordered distribution of dopants amongst the available sites.

Assessing our spin density calculations, we will first discuss the effect of Mo doping in V sites. At 6.25 at% doping, the effect is similar in both t-$BiVO_4$ (Fig. 9) and m-$BiVO_4$ (Fig. S10†), with the $4d^1$ electron of Mo localising primarily on the Mo dopant site, within a single d-orbital with a distinct distribution of charge. At 12.5 at% doping in m-$BiVO_4$, the situation is similar, with the $4d^1$ electron remaining quite localised to Mo (Fig. S13†). However, at 12.5 at% doping in t-$BiVO_4$, a significant change is seen, with the $4d^1$ electron being completely transferred from Mo to V 3d orbitals that lie in the [001] Miller plane (Fig. 10). The exact concentration at which the delocalisation occurs will be sensitive to the treatment of electronic self-interaction and to the particular distribution of dopants in the structure. Nevertheless, it is not unreasonable to conclude that as the dopant concentration approaches 12.5 at% there is a transition from a strongly correlated insulating state to a delocalised semiconductor. This inference is further supported by our XRD data (Fig. 2), in which the peak at ~31° 2Θ, which corresponds to diffraction in the [004] plane, increases in intensity with Mo doping, and is significantly more pronounced in the 6% Mo–$BiVO_4$ sample. This is likely to be a result of the increased electron density in the [001] plane with Mo doping, as X-ray diffraction correlates with electron density.

Regarding the effect of Mo doping in Bi sites, at both 6.25 and 12.5 at% doping in both t-$BiVO_4$ and m-$BiVO_4$, the $4d^3$ electrons of Mo remain localised to Mo dopant sites, filling several d-orbitals to achieve a near even distribution of charge around the ion, with some spill-over seen onto neighbouring O and nearby V sites. With increased levels of Mo doping, the spillover onto neighbouring O and nearby V sites increases, however, we do not observe a transition to a delocalised state and charge remains primarily localised to Mo dopant sites.

3.4.2. Density of states. Full scale PDOS calculations are shown in Fig. S17 and S18† for all Mo doped t-$BiVO_4$ and m-$BiVO_4$ structures, respectively. Included in these figures are atom projections for all the doped structures and the projections of the specific orbitals that form the valence and conduction band in t-$BiVO_4$ and m-$BiVO_4$.[90,91] As seen in previous work,[92] in both t-$BiVO_4$ and m-$BiVO_4$, there are notable contributions from the Bi 6s and O 2p atomic orbitals that form the VBM and V 3d atomic orbitals that form the CBM. Of particular importance to the function of photoelectrodes is the bandgap energy and material conductivity. The PDOS in the bandgap region for all Mo doped t-$BiVO_4$ and m-$BiVO_4$ structures is shown in Fig. 11, with the computed energy gaps summarised in Table 5. In line with previous studies, the valence band maximum (VBM) region of all structures was primarily composed of O 2p orbitals, partially hybridised with Bi 6s orbitals, and the conduction band minimum (CBM) region of all structures was primarily composed of V 3d orbitals. This is consistent with a simple ionic picture of Bi^{3+} $d^{10}s^2$ and V^{5+} d^0. The calculated band structures of t-$BiVO_4$ and m-$BiVO_4$ show that the lowest bandgap energy transitions are both indirect (Fig. S19†). The calculated bandgap energies of the undoped t-$BiVO_4$ and m-$BiVO_4$ structures were ~2.66 and ~2.69 eV, respectively (Fig. 11a). The calculated bandgap is determined to be indirect in both cases as the top of the valence band and bottom of the conduction band were located at different points in reciprocal space, as demonstrated by the band structures (Fig. S19†). This agrees with recent articles which consistently show the bandgap in $BiVO_4$ to be indirect.[93,94] Also, our experimentally determined value for the indirect bandgap transition in m-$BiVO_4$ (Table 1) was close in value (~2.55 eV) to that we calculated (~2.69 eV), and was in line with previous experimental observations for $BiVO_4$.[95] The computed band gaps are sensitive to the electronic self-interaction which we emphasise

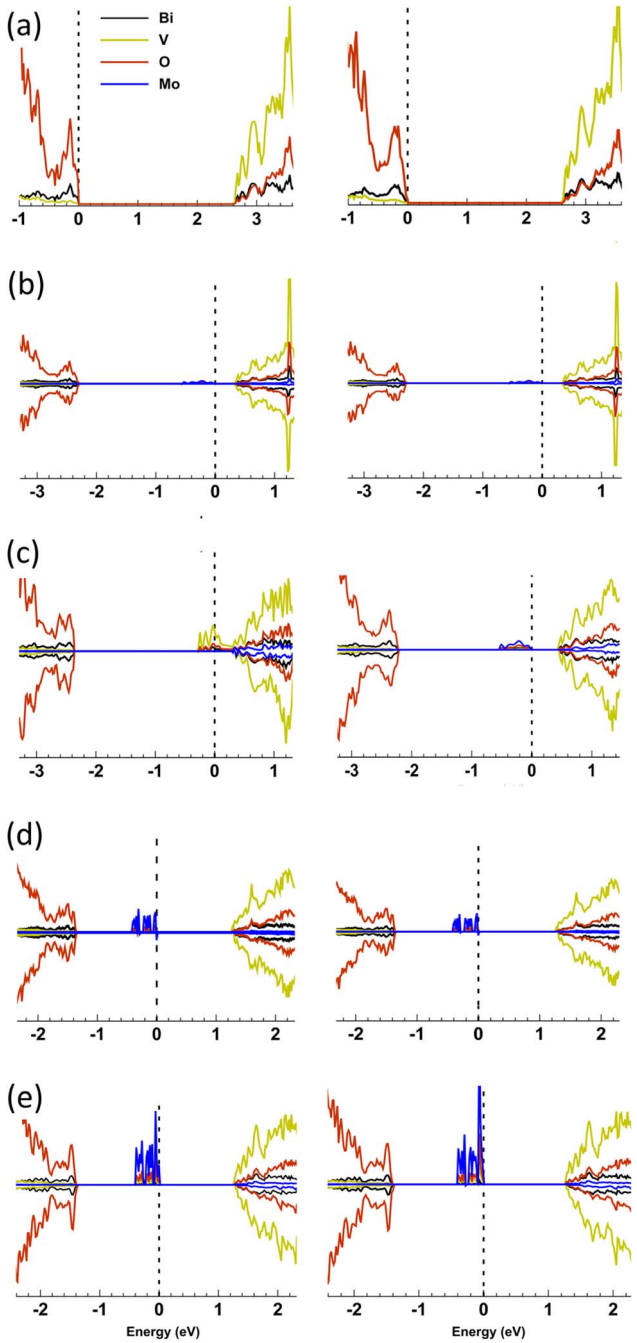

Fig. 11 Comparison of the PDOS for (left) t-$BiVO_4$ and (right) m-$BiVO_4$ host structures for (a) undoped, (b) 6.25 at% Mo in a V site, (c) 12.5 at% Mo in a V site, (d) 6.25 at% Mo in a Bi site, and (e) 12.5 at% Mo in a Bi site. For each host structure, the VBM, formed primarily by O orbitals, are plot at the same position to one another. The PDOS are drawn for energies ~1 eV below the VBM up to ~1 eV above the CBM, which is formed primarily by V orbitals. The dashed line represents the highest occupied state in each structure.

is here determined by the 10% admixture of Fock exchange in the PBE0 functional.[96]

When the t-$BiVO_4$ and m-$BiVO_4$ structures were doped with Mo at either V or Bi sites (with the exception of 12.5 at% doping in V sites in t-$BiVO_4$) there is no substantial change in the bandgap energy. The electronic structure of the doped state, however, does depend critically on the doping concentration. At 6.25 at% Mo doping on the V^{5+}-site an upper band gap state of predominantly Mo character is formed ~0.6 eV below the CBM with a width of ~0.4 eV is formed (Fig. 11b). The state is of pure spin character and makes carriers available for thermally activated or hoping conductivity. The state may be characterised as a semi-localised Mo^{5+} $4d^1$ orbital with the localisation attributable to strong on-site correlation. At 12.5 at% Mo doping in t-$BiVO_4$ this state is ionised to Mo^{6+} d^0 and a band of V-derived states at the CBM are occupied producing a half metallic phase, as the kinetic energy of delocalisation in the V-d-band becomes the dominant energy scale (Fig. 11c). Analysis of the resultant spin density reveals that the charge is distributed over several neighbouring V sites, and is therefore likely to produce band-like electron conductivity. This delocalisation does not occur in m-$BiVO_4$ at 12.5 at% Mo doping, but is highly likely to do so at higher dopant concentrations. Doping at the Bi^{3+} site produces a localised Mo^{3+} $4d^3$ pure spin band centred some 1.4 eV below the CBM for both structures and concentrations considered.

Some consistent themes were seen with Mo dopants replacing V and Bi sites. Mo doping in V sites resulted in a more significant shift in the highest occupied state (HOS) energy from the VBM to ~2.2–2.3 eV above the VBM, whereas Mo doping in Bi sites resulted in a less significant shift in HOS energy from the VBM to ~1.1–1.3 eV above the VBM. This indicated that Mo doping in V sites will result in a more conductive material at room temperature than Mo doping in Bi sites. Also, Mo doping in both V and Bi sites resulted in the formation of mid-gap states, which were primarily composed of Mo 4d orbitals. These mid-gap states were closer to the CBM where Mo replaced V (~0.3–0.4 eV) than where Mo replaced Bi (~1.2 eV). Where Mo replaced Bi sites, the higher level of associated electrons on Mo (*i.e.* $4d^3$) resulted in a larger contribution of Mo 4d orbitals to the mid-gap state as compared with cases where Mo replaced V sites, which possessed a lower level of associated electrons on Mo (*i.e.* $4d^1$). An exception was seen where Mo dopants replaced V sites at a concentration of 12.5 at%, where the mid-gap Mo 4d states merged with the CBM, resulting in the formation of a degenerate semiconductor where the HOS level resided in the conduction band (CB). Interestingly, electronic charge previously associated with Mo 4d orbitals was transferred onto V 3d orbitals that formed the CBM.

Our experimental findings indicated that Mo dopants relaced V sites, and at a doping level of ~9.6 at% of Mo in V sites, we saw our most active photoanode, where the performance under front irradiation was the most markedly improved. This was evidence that the transport of photogenerated electron carriers in $BiVO_4$ was improved upon Mo doping, reaching an optimum value at ~9.6 at%. This was in line with our computational studies, which indicated conductivity would significantly increase in Mo doped systems, due to a raising of the highest occupied state from the VBM to a filled mid-gap state (by ~2.27 eV where V was replaced by Mo at a doping level of 6.25 at%). Importantly, our computational studies also showed that high levels of Mo doping results in the

Table 5 Table listing and comparing the calculated PDOS energy gaps (valence band maximum [VBM] to highest occupied state [HOS]; [HOS] to conduction band minimum [CBM]; VBM to CBM) for the undoped and Mo-doped t-$BiVO_4$ and m-$BiVO_4$ structures studied herein

Structure	Dopant site	Doping level (at%)	Energy gaps (eV)		
			VBM to HOS	HOS to CBM	VBM to CBM
t-$BiVO_4$	n/a	0	0	2.6639	2.6639
	V	6.25	~2.27	0.3483	2.6717
		12.5	~2.28	No gap[a]	2.1451[b]
	Bi	6.25	~1.27	1.244	2.6609
		12.5	~1.28	1.2523	2.6873
m-$BiVO_4$	n/a	0	0	2.6943	2.6943
	V	6.25	~2.24	0.3672	2.6770
		12.5	~2.20	0.4275	2.6626
	Bi	6.25	~1.17	1.2431	2.6610
		12.5	~1.18	1.2473	2.6879

[a] The HOS resides above the CBM. [b] Degenerate semiconductor; transition from VBM to HOS residing above the CBM.

formation of a degenerate semiconductor, with metal-like conductivity. This would result in a significant increase in the donor density, increasing the probability of electron–hole recombination, and reducing the degree of band-bending on the material, which would both be deleterious to the performance of the photoanode. This finding was also in line with our experiments, where at higher levels of Mo doping of ~12.7 at%, a reduction in performance was observed.

3.4.3. Comparisons with previous DFT studies on Mo-doped $BiVO_4$. Various dopants in bulk $BiVO_4$ structures have previously been studied by DFT methods, including d-block, p-block and f-block dopants,[97–99] as well as point defect vacancies,[100] surface structures[101] and heterostructures.[102,103] Herein, our discussion will primarily focus on studies where Mo-doping was considered.

It is often argued that m-$BiVO_4$ produces the most active photocatalyst.[92] However, herein, both theoretical and experimental evidence has been presented for a transition from m-$BiVO_4$ to t-$BiVO_4$ induced by doping with Mo. Our XPS data and first principles thermodynamics also suggest that Mo replaces V sites in the host structure. Our experimental studies also showed that optimal performance for use as a photoanode in water splitting was achieved in our 6% Mo : $BiVO_4$ sample, which was of the t-$BiVO_4$ structure and contained an Mo : V doping level of ~9.6 at%. Our calculations showed that Mo doping of V sites, in general, did not significantly alter the fundamental bandgap, but created a thermally accessible donor band at low doping concentration and then a semi-metallic state at higher concentration, thus significantly enhancing electron mobility. This picture is consistent with our experimental results, where Mo doping did not alter the bandgap energy but increased electron conductivity which was seen to be responsible for the improved photoelectrochemical performance.

Previous DFT studies of Mo-doped $BiVO_4$ have predominantly applied the generalized gradient approximation alongside a Hubbard U value correction (GGA + U) to carry out first principles calculations of this system. Herein, we avoided using an *ad hoc* correction to the GGA functional by adopting the hybrid PBE0 functional with a Hartree–Fock mixing at 10%. This leads to a more consistent prediction of the structure, electronic structure and bandgap of $BiVO_4$ than that of standard GGA methods, which often fails to describe defect states accurately.[96] It should also be noted that most previous studies have primarily focussed on Mo doping of the m-$BiVO_4$ structure, with no previous studies, to the authors knowledge, of the ground state structure identified here of Mo doping in the t-$BiVO_4$ structure.

Using the GGA + U functional (U correction for V, Mo and W was 5.0 eV for all cases), Pasumarthi *et al.* studied charge carrier transport in Mo doped $BiVO_4$, where Mo was substituted for V. Doping resulted in the addition of one electron per dopant atom, where these electrons were seen to be mobile and able to hop through the structure with an energy requirement of ~–0.73 k_BT.[93] Zhao *et al.* used an uncorrected GGA functional to study the effect of doping m-$BiVO_4$ in V sites at 6.25 at%, with a range of transitions metals explored, including Mo.[104] They observed a unit cell volume increase of 2.35 A^3, which was similar to that in our calculations of ~2.34 A^3. No significant change in bandgap energy seen with Mo doping (~2.048 eV), and no mid-gap state was observed in their PDOS. Changes in hole and electron masses were observed with Mo doping, with the hole mass reducing from 0.41 to 0.34 m_0, and the electron mass increasing from 0.55 to 1.16 m_0, which was indicative of a decrease in electron mobility in this system. Using a GGA + U functional (U correction for V, Mo and W = 2.7, 2.3 and 2.1 eV, respectively), Zhang *et al.* studied the effect of Mo and W doping and co-doping of V and Bi sites in m-$BiVO_4$ at 6.25 and 12.5 at%.[105] They observed mid-gap states where Mo replaced Bi sites, and degenerate states that filled the CB when Mo replaced V sites. At 6.25 at% Mo doping of V sites, a reduction in the bandgap energy of 2.30 to 2.23 eV was observed. Shi *et al.* applied the GGA + U functional to study Mo and W co-doping of V sites in m-$BiVO_4$ at 12.5 and 25 at% (U correction for V, Mo and W = 2.7, 2.3 and 2.1 eV, respectively).[94] Higher levels of Mo doping led to a widening of the bandgap from ~2.1 to ~2.3 eV, with Mo 4d states primarily forming the CBM as opposed to W 5d states. Park *et al.* utilised a GGA + U functional

to study Mo doping of V sites in m-$BiVO_4$ (U correction for V, Mo and W = 2.7, 2.3 and 2.1 eV, respectively).[106] In their study they observed a mid-gap state ~1 eV above the VBM, where excess charge was primarily transferred from Mo to V sites. Li *et al.* applied a GGA + U functional to study Mo-doped $BiVO_4$ (U correction for V = 3.0 eV and Mo = 2.7 eV).[107] They observed bandgaps of 2.08 and 2.01 eV for the undoped and Mo-doped $BiVO_4$, respectively. With Mo-doping, they also observed an increase in n-type character and the formation of a shallow, filled mid-gap state beneath the CBM. And Ahmed *et al.* applied a GGA + U functional to study Mo-doping in m-$BiVO_4$ at 6.25 at% (U corrections for Bi, V, O and M of 4.8, 3.1, 2.0 and 2.3 eV, respectively).[108] Like several previous studies highlighted above, they found that Mo doping introduces a shallow filled spin-up impurity state near the CBM. They also found that the bandgap of the undoped material (2.51 eV) did not alter significantly upon Mo doping (2.52 eV).

Similar to our calculations herein, the hybrid HSE exchange-correlation functional was used by Laraib *et al.* to study the effect of doping in t-$BiVO_4$ and m-$BiVO_4$.[109] In their work, they simulated an n-doping of up to 0.25 electrons per formula unit by adding electrons and a homogeneous charge compensating background. They found that the resultant electron addition states localised on V sites in both structures, and that the t-$BiVO_4$ structure was less stable than the m-$BiVO_4$ structure. In contrast to the current work, they reported a computed electronic bandgap ~0.9 eV higher than that calculated herein. Ding *et al.* also applied the hybrid HSE exchange-correlation functional in their study of Mo-doping in m-$BiVO_4$.[96] Similar to our work, they investigated Mo dopants substituting either V or Bi sites at a concentration of 6.25 at%. They found that the formation energy of Mo-doped m-$BiVO_4$ was lower when Mo substituted V sites as opposed to Bi sites. For the case of Mo doping in tetrahedral V sites, the average Mo–O bond length was ~1.79 Å (~0.05 Å lower than our calculations) and for the case of Mo doping in cubic Bi sites the average Mo–O bond length was ~2.16 Å (~0.29 Å lower than our calculations). They used these bond lengths as a measure of the Mo valency with the implication of Mo^{6+} at V sites and Mo^{3+} at Bi sites. Ding *et al.*[96] also reported that optimisation with the GGA functional produces no mid-gap state when Mo replaces V sites, however, a mid-gap state is formed when Mo replaced Bi sites. Upon recalculating the electronic structure using the HSE functional, a mid-gap state is formed upon doping into V sites. They reported that the bandgap of m-$BiVO_4$ increased from ~2.08 eV to ~2.14 eV upon Mo doping V sites. Again these gaps are significantly lower than those reported here (~2.69 to ~2.68 eV, respectively) which can be attributed to the differing treatments of the Fock exchange contribution.

Using the hybrid PBE0 functional (with 10% Fock exchange mixing) our calculations provide a more consistent description of the electronic structure, which corresponds more closely to the observed optical bands gaps and transport properties seen experimentally. In addition, by considering both the m-$BiVO_4$ and t-$BiVO_4$ structures at 6.25 and 12.5 at% Mo doping, insights into the effect of doping induced changes in phase stability were also obtained, providing computational support for the observed phase change from m-$BiVO_4$ seen with no doping to t-$BiVO_4$ upon doping with Mo.

4 Conclusions

Herein, a new AA-CVD route to Mo-doped $BiVO_4$ photoanodes is developed. By studying a range of Mo precursor doping levels (0 to 12% Mo: V), an optimum photoanode for driving photocatalytic water oxidation was found at 6% Mo precursor doping, which corresponded to an actual Mo : V doping level of ~9.6 ± 0.4%. XPS indicated that these Mo dopants inserted the host structure as Mo^{6+} states, replacing V^{5+} sites. The PEC water oxidation performance was favourable compared to leading Mo-doped $BiVO_4$ materials; with the 6% Mo : $BiVO_4$ sample showing a J_{on} of ~0.6 V_{RHE} and TSP of ~1.79 mA cm^{-2} at 1.23 V_{RHE} and 1 sun irradiance under front irradiation. By comparing differences in PEC water oxidation performance under front and back irradiation, it was concluded that Mo-doping herein improved electron carrier transport and extraction in the host material by a factor of between 4 and 5, but did not significantly impact hole carrier behaviour. Importantly, Mo-doping was found to induce a phase change from monoclinic clinobisvanite (m-$BiVO_4$), in undoped $BiVO_4$, to tetragonal scheelite (t-$BiVO_4$). Using DFT, the effect of Mo-doping on the structural and electronic properties was studied using a global hybrid exchange-correlation functional PBE0-10. Both t-$BiVO_4$ and m-$BiVO_4$ structures were investigated, with Mo dopants replacing V or Bi sites at 6.25 and 12.5 at%, with respect to the metal site being replaced. Mo doping of V sites led to an expansion of the lattice, whereas Mo doping of Bi sites led to a contraction, and supported our conclusion from experimental work that Mo dopants substituted V sites. In agreement with our observations, Mo doping of V sites in t-$BiVO_4$ at 6.25 at% produced a lower energy than in m-$BiVO_4$ (~2.33 meV lower per dopant). At 12.5 at% the energy difference is negligible. Doping at both Bi and V sites resulted in the formation of localised mid-gap states primarily composed of Mo 4d orbitals, with the exception of 12.5 at% Mo doping of V sites in t-$BiVO_4$, where the states merge with the conduction band minimum, forming a degenerate semiconductor with electrons distributed over multiple V 3d ion sites. All cases of doping raised the highest occupied state and likely increased the conductivity of the system.

The findings herein not only support current understanding surrounding the effect of Mo-doping on the electron conductivity in $BiVO_4$, but provide further insight on the subtle structural changes that can occur and how this impacts the density of states. Moreover, the development of a new, scalable synthetic route to high performance Mo-doped $BiVO_4$ photoanodes may influence the future commercialisation of this technology.

Data availability

The data supporting this article have been included as part of the ESI.†

Conflicts of interest

There are no conflicts to declare.

Acknowledgements

A. K. thanks the EPSRC for a Programme Grant (EP/W017075/1) and the Royal Society for an Equipment Grant (RSG\R1\180434). B. T. thanks Imperial College London for support from the President's PhD Scholarship. We wish to acknowledge the use of the EPSRC funded Physical Sciences Data-science Service hosted by the University of Southampton and STFC under grant number EP/S020357/1. Lee Tooley, Steve Atkins and Stefanos Karapanagiotidis are thanked for constructing and maintaining our chemical vapour deposition apparatus. S. D. P. thanks the Royal Society for support for a University Research Fellowship (URF\R1\191458) and Research Grant (RG\R2\232264), and to Dr Ivan Prokes for technical support of 51V NMR spectroscopy. N. M. H is grateful for computational support from the UK national high performance computing service, ARCHER2, for which access was obtained *via* the UKCP consortium and funded by EPSRC grant ref EP/X035891/1.

References

1 V. Masson-Delmotte, P. Zhai, A. Pirani, S. L. Connors, C. Péan, S. Berger, N. Caud, Y. Chen, L. Goldfarb, M. I. Gomis, M. Huang, K. Leitzell, E. Lonnoy, J. B. R. Matthews, T. K. Maycock, T. Waterfield, O. Yelekçi, R. Yu and B. Zhou, The Physical Science Basis. Contribution of Working Group I to the Sixth Assessment Report of the Intergovernmental Panel on Climate Change, 2021, **https://www.ipcc.ch/report/sixth-assessment-report-working-group-i/**, accessed August 2nd 2024.

2 I. Prentice, G. Farquhar, M. Fasham, M. Goulden, M. Heimann, V. Jaramillo, H. Kheshgi, C. Le Quéré, R. Scholes and D. Wallace, The carbon cycle and atmospheric carbon dioxide, *Climate Change 2001: the Scientific Basis*, Cambridge University Press, 2001, pp. 183–237.

3 V. Masson-Delmotte, P. Zhai, H. O. Pörtner, D. Roberts, J. Skea, P. R. Shukla, A. Pirani, W. Moufouma-Okia, C. Péan, R. Pidcock, S. Connors, J. B. R. Matthews, Y. Chen, X. Zhou, M. I. Gomis, E. Lonnoy, T. Maycock, M. Tignor and T. Waterfield, Impacts of 1.5°C Global Warming on Natural and Human Systems, Global warming of 1.5°C. An IPCC Special Report on the impacts of global warming of 1.5°C above pre-industrial levels and related global greenhouse gas emission pathways, in *The Context of Strengthening the Global Response to the Threat of Climate Change*, 2018, **https://www.ipcc.ch/site/assets/uploads/sites/2/2019/02/SR15_Chapter3_Low_Res.pdf** accessed 2nd August 2024.

4 M. New, D. Liverman, H. Schroeder, H. Schroder and K. Anderson, *Philos. Trans. A Math. Phys. Eng. Sci.*, 2011, **369**, 6–19.

5 D. Gust, D. Kramer, A. Moore, T. A. Moore and W. Vermaas, *MRS Bull.*, 2008, **33**, 383–387.

6 F. E. Osterloh, *Chem. Mater.*, 2008, **20**, 35–54.

7 B. Moss, O. Babacan, A. Kafizas and A. Hankin, *Adv. Energy Mater.*, 2021, **11**, 2003286.

8 J. H. Kim, D. Hansora, P. Sharma, J. W. Jang and J. S. Lee, *Chem. Soc. Rev.*, 2019, **48**, 1908–1971.

9 Y. Pihosh, I. Turkevych, K. Mawatari, J. Uemura, Y. Kazoe, S. Kosar, K. Makita, T. Sugaya, T. Matsui, D. Fujita, M. Tosa, M. Kondo and T. Kitamori, *Sci. Rep.*, 2015, **5**, 11141.

10 D. K. Lee and K.-S. Choi, *Nat. Energy*, 2018, **3**, 53–60.

11 M. Huang, W. Lei, M. Wang, S. Zhao, C. Li, M. Wang and H. Zhu, *J. Mater. Chem. A*, 2020, **8**, 3845–3850.

12 I. Y. Ahmet, Y. Ma, J.-W. Jang, T. Henschel, B. Stannowski, T. Lopes, A. Vilanova, A. Mendes, F. F. Abdi and R. van de Krol, *Sustain. Energy Fuels*, 2019, **3**, 2366–2379.

13 A. Kafizas and I. P. Parkin, Materials for a Sustainable Future, *Chapter 20 – Glass and New Technologies*, The Royal Society of Chemistry, Cambridge, 1st edn, 2012.

14 P. Brack, J. S. Sagu, T. A. N. Peiris, A. McInnes, M. Senili, U. Wijayantha, F. K. G. Marken and E. Selli, *Chem. Vap. Deposition*, 2015, **21**, 41–45.

15 S. N. F. Mohd-Nasir, M. A. Mat-Teridi, M. Ebadi, J. S. Sagu, M. Y. Sulaiman, N. A. Ludin and M. A. Ibrahim, *Phys. Status Solidi A*, 2015, **212**, 2910–2914.

16 E. Alarcón-Lladó, L. Chen, M. Hettick, N. Mashouf, Y. Lin, A. Javey and J. W. Ager, *Phys. Chem. Chem. Phys.*, 2014, **16**, 1651–1657.

17 P. S. Archana, Z. Shan, S. Pan and A. Gupta, *Int. J. Hydrogen Energy*, 2017, **42**, 8475–8485.

18 Y. Park, K. J. McDonald and K.-S. Choi, *Chem. Soc. Rev.*, 2013, **42**, 2321–2337.

19 M. A. Gaikwad, U. P. Suryawanshi, U. V Ghorpade, J. S. Jang, M. P. Suryawanshi, J. H. Kim, M. A. Gaikwad, U. P. Suryawanshi, J. S. Jang, J. H. Kim, U. V Ghorpade and M. P. Suryawanshi, *Small*, 2022, **18**, 2105084.

20 Innovation Challenge 5: Converting Sunlight into Fuels and Chemicals Roadmap 2020 – 2050, Mission Innovation, 2019, **https://mission-innovation.net/our-work/innovation-challenges/converting-sunlight/**, accessed 2nd August 2024.

21 N. Österbacka, F. Ambrosio and J. Wiktor, *J. Phys. Chem. C*, 2022, **126**, 2960–2970.

22 S. Chen and L.-W. Wang, *Chem. Mater.*, 2012, **24**, 3659–3666.

23 Y. Ma, S. R. Pendlebury, A. Reynal, F. Le Formal and J. R. Durrant, *Chem. Sci.*, 2014, **5**, 2964–2973.

24 A. Kafizas, R. Godin and J. R. Durrant, *Semiconduct. Semimet.*, 2017, **97**, 3–46.

25 Y. Ma, C. A. Mesa, E. Pastor, A. Kafizas, L. Francàs, F. Le Formal, S. R. Pendlebury and J. R. Durrant, *ACS Energy Lett.*, 2016, **1**, 618–623.

26 K. T. Butler, B. J. Dringoli, L. Zhou, P. M. Rao, A. Walsh and L. V. Titova, *J. Mater. Chem. A*, 2016, **4**, 18516–18523.

27 F. F. Abdi, T. J. Savenije, M. M. May, B. Dam and R. Van De Krol, *J. Phys. Chem. Lett.*, 2013, **4**, 2752–2757.

28 G. Talasila, S. Sachdev, U. Srivastva, D. Saxena and S. S. V. Ramakumar, *Energy Rep.*, 2020, **6**, 1963–1972.
29 M. Tayebi and B. K. Lee, *Renew. Sustain. Energy Rev.*, 2019, **111**, 332–343.
30 R. P. Antony, P. S. Bassi, F. F. Abdi, S. Y. Chiam, Y. Ren, J. Barber, J. S. C. Loo and L. H. Wong, *Electrochim. Acta*, 2016, **211**, 173–182.
31 H. Jung, S. Y. Chae, H. Kim, B. K. Min and Y. J. Hwang, *Catal. Commun.*, 2016, **75**, 18–22.
32 M. W. Kim, K. Kim, T. Y. Ohm, B. Joshi, E. Samuel, M. T. Swihart, H. Yoon, H. Park and S. S. Yoon, *J. Alloys Compd.*, 2017, **726**, 1138–1146.
33 A. J. E. Rettie, H. C. Lee, L. G. Marshall, J. F. Lin, C. Capan, J. Lindemuth, J. S. McCloy, J. Zhou, A. J. Bard and C. B. Mullins, *J. Am. Chem. Soc.*, 2013, **135**, 11389–11396.
34 L. Yang, Y. Xiong, W. Guo, J. Guo, D. Gao, Y. Zhang and P. Xiao, *Electrochim. Acta*, 2017, **256**, 268–277.
35 Y. Bu, J. Tian, Z. Chen, Q. Zhang, W. Li, F. H. Tian and J. P. Ao, *Adv. Mater. Interfaces*, 2017, **4**, 1–9.
36 J. A. Seabold, K. Zhu and N. R. Neale, *Phys. Chem. Chem. Phys.*, 2014, **16**, 1121–1131.
37 M. Rohloff, B. Anke, S. Zhang, U. Gernert, C. Scheu, M. Lerch and A. Fischer, *Sustain. Energy Fuels*, 2017, **1**, 1830–1846.
38 A. Iwase, S. Ikeda and A. Kudo, *Chem. Lett.*, 2017, **46**, 651–654.
39 Y. Qiu, S. Fan, Y. Zhang, W. Liu, W. Chen, G. Zhou, P.-C. Hsu, R. Zhang, Z. Liang and Y. Cui, *Sci. Adv.*, 2016, **2**, e1501764.
40 W. Luo, J. Wang, X. Zhao, Z. Zhao, Z. Li and Z. Zou, *Phys. Chem. Chem. Phys.*, 2013, **15**, 1006–1013.
41 S. K. Pilli, T. E. Furtak, L. D. Brown, T. G. Deutsch, J. A. Turner and A. M. Herring, *Energy Environ. Sci.*, 2011, **4**, 5028–5034.
42 L. Chen, F. M. Toma, J. K. Cooper, A. Lyon, Y. Lin, I. D. Sharp and J. W. Ager, *ChemSusChem*, 2015, **8**, 1066–1071.
43 M. Huang, J. Bian, W. Xiong, C. Huang and R. Zhang, *J. Mater. Chem. A*, 2018, **6**, 3602–3609.
44 S. Tokunaga, H. Kato and A. Kudo, *Chem. Mater.*, 2001, **13**, 4624–4628.
45 D. T. T. Trinh, W. Khanitchaidecha, D. Channei and A. Nakaruk, *Res. Chem. Intermed.*, 2019, **45**, 5217–5259.
46 M. Schüler, S. Barthel, T. Wehling, M. Karolak, A. Valli and G. Sangiovanni, *Eur. Phys. J. Spec. Top.*, 2017, **226**, 2615–2640.
47 F. Corà, *Mol. Phys.*, 2005, **103**, 2483–2496.
48 C. Adamo and V. Barone, *J. Chem. Phys.*, 1999, **110**, 6158–6170.
49 J. Muscat, A. Wander and N. M. Harrison, *Chem. Phys. Lett.*, 2001, **342**, 397–401.
50 C. Franchini, R. Podloucky, J. Paier, M. Marsman and G. Kresse, *Phys. Rev. B: Condens. Matter Mater. Phys.*, 2007, **75**, 195128.
51 A. J. Garza and G. E. Scuseria, *J. Phys. Chem. Lett.*, 2016, **7**, 4165–4170.
52 Home | Physical Sciences Data science Service, **https://www.psds.ac.uk/**, accessed 2nd August 2024.
53 B. H. Toby, *J. Appl. Crystallogr.*, 2001, **34**, 210–213.
54 RRUFF database of Raman spectroscopy, X-ray diffraction and chemistry of minerals, **http://rruff.info/**, accessed 2nd August 2024.
55 Casa Software Ltd, **http://www.casaxps.com/**, accessed 2nd August 2024.
56 M. Wang, A. Kafizas, S. Sathasivam, M. O. Blunt, B. Moss, S. Gonzalez-Carrero and C. J. Carmalt, *Appl. Catal., B*, 2023, **331**, 122657.
57 F. Pinto, A. Wilson, B. Moss and A. Kafizas, *J. Phys. Chem. C*, 2022, **126**, 871–884.
58 R. Dovesi, C. Roetti, C. Freyria-Fava, E. Aprà, V. R. Saunders and N. M. Harrison, Ab initio Hartree-Fock treatment of ionic and semi-ionic compounds: state of the art, *Philos. Trans. R. Soc., A*, 1992, **341**, 203–210.
59 R. Dovesi, A. Erba, R. Orlando, C. M. Zicovich-Wilson, B. Civalleri, L. Maschio, M. Rérat, S. Casassa, J. Baima, S. Salustro and B. Kirtman, *Wiley Interdiscip. Rev. Comput. Mol. Sci.*, 2018, **8**, e1360.
60 R. Weihrich and I. Anusca, *Z. Anorg. Allg. Chem.*, 2006, **632**, 335–342.
61 M. F. Peintinger, D. V. Oliveira and T. Bredow, *J. Comput. Chem.*, 2013, **34**, 451–459.
62 T. Bredow, K. Jug and R. A. Evarestov, *Phys. Status Solidi B*, 2006, **243**, R10–R12.
63 J. Laun, D. Vilela Oliveira and T. Bredow, *J. Comput. Chem.*, 2018, **39**, 1285–1290.
64 J. W. E. Mariathasan, R. M. Hazen and L. W. Finger, *Phase Transitions*, 1986, **6**, 165–173.
65 A. W. Sleight, H. y. Chen, A. Ferretti and D. E. Cox, *Mater. Res. Bull.*, 1979, **14**, 1571–1581.
66 H. J. Monkhorst and J. D. Pack, *Phys. Rev. B*, 1976, **13**, 5188.
67 J. D. Pack and H. J. Monkhorst, *Phys. Rev. B.*, 1977, **16**, 1748.
68 C. Sotelo-Vazquez, N. Noor, A. Kafizas, R. Quesada-Cabrera, D. O. Scanlon, A. Taylor, J. R. Durrant and I. P. Parkin, *Chem. Mater.*, 2015, **27**, 3234.
69 R. Grybo, A. Samotus, N. Popova and K. Bogolitsyn, *Transition Met. Chem.*, 1997, **22**, 61–64.
70 F. Jiang, O. P. Anderson, S. M. Miller, J. Chen, M. Mahroof-Tahir and D. C. Crans, *Inorg. Chem.*, 1998, **37**, 5439–5451.
71 S. Byun, G. Jung, Y. Shi, M. Lanza and B. Shin, *Adv. Funct. Mater.*, 2020, **30**, 1806662.
72 J. D. Bierlein and A. W. Sleight, *Solid State Commun.*, 1975, **16**, 69–70.
73 J. W. E. Mariathasan, R. M. Hazen and L. W. Finger, *Phase Transitions*, 1986, **6**, 165–173.
74 R. L. Frost, D. a. Henry, M. L. Weier and W. Martens, *J. Raman Spectrosc.*, 2006, **37**, 722–732.
75 S. S. Mali, G. R. Park, H. Kim, H. H. Kim, J. V. Patil and C. K. Hong, *Nanoscale Adv.*, 2019, **1**, 799–806.
76 V. I. Merupo, S. Velumani, K. Ordon, N. Errien, J. Szade and A. H. Kassiba, *CrystEngComm*, 2015, **17**, 3366–3375.
77 J. Kasperkiewicz, J. A. Kovacich and D. Lichtman, *J. Electron Spectrosc. Relat. Phenom.*, 1983, **32**, 123–132.

78 T. Lindblad, B. Rebenstorf, Z. G. Yan and S. L. T. Andersson, *Appl. Catal., A*, 1994, **112**, 187–208.
79 B. Folkesson and P. Sundberg, *Spectrosc. Lett.*, 1987, **20**, 193–200.
80 *Average Matrix Relative Sensitivity Factors (AMRSFs) for X-ray Photoelectron Spectroscopy (XPS)*, National Physics Laboratory, 2006, **https://www.npl.co.uk/research/surface-technology/xpsamrsf**, accessed 2nd August 2024.
81 J. B. Gilbert, M. F. Rubner and R. E. Cohen, *Proc. Natl. Acad. Sci. U.S.A.*, 2013, **110**, 6651–6656.
82 M. Shimoda, T. Hirata, K. Yagisawa, M. Okochi and A. Yoshikawa, *J. Mater. Sci. Lett.*, 1989, **8**(9), 1089–1091.
83 G. Seifert, J. Finster and H. Müller, *Chem. Phys. Lett.*, 1980, **75**, 373–377.
84 E. G. Il'in, A. G. Beirakhov, Y. A. Teterin, K. I. Maslakov and A. Y. Teterin, *Inorg. Mater.*, 2017, **53**(6), 602–612.
85 K. Ding, B. Chen, Z. Fang and Y. Zhang, *Theor. Chem. Acc.*, 2013, **132**, 1–7.
86 R. Crespo-Otero and A. Walsh, *J. Phys. Chem. Lett.*, 2015, **6**, 2379–2383.
87 C. Ràfols i Bellés, S. Selim, N. M. Harrison, E. A. Ahmad and A. Kafizas, *Sustain. Energy Fuels*, 2019, **3**, 264–271.
88 Y. Park, D. Kang and K. S. Choi, *Phys. Chem. Chem. Phys.*, 2014, **16**, 1238–1246.
89 R. D. Shannon, *Acta Crystallogr. A*, 1976, **32**, 751–767.
90 G. Wang, L. Gong, Z. Li, B. Wang, W. Zhang, B. Yuan, T. Zhou, X. Long and A. Kuang, *Phys. Chem. Chem. Phys.*, 2020, **22**, 9587–9592.
91 J. Wang, X. Li, Y. You, X. Yang, Y. Wang and Q. Li, *Nanotechnology*, 2018, **29**, 365401.
92 A. Walsh, Y. Yan, M. N. Huda, M. M. Al-Jassim and S.-H. Wei, *Chem. Mater.*, 2009, **21**, 547–551.
93 V. Pasumarthi, T. Liu, M. Dupuis and C. Li, *J. Mater. Chem. A*, 2019, **7**, 3054–3065.
94 J. Shi, W. Zhang and Q. Gu, *Solid State Commun.*, 2022, **351**, 114794.
95 S. Tokunaga, H. Kato and A. Kudo, *Chem. Mater.*, 2001, **13**, 4624–4628.
96 K. Ding, B. Chen, Z. Fang, Y. Zhang and Z. Chen, *Phys. Chem. Chem. Phys.*, 2014, **16**, 13465.
97 G. V. Govindaraju, J. M. Morbec, G. A. Galli and K.-S. Choi, *J. Phys. Chem. C*, 2018, **122**, 19416–19424.
98 A. Ngoipala, L. Ngamwongwan, I. Fongkaew, S. Jungthawan, P. Hirunsit, S. Limpijumnong and S. Suthirakun, *J. Phys. Chem. C*, 2020, **124**, 4352–4362.
99 S. N. F. M. Nasir, H. Ullah, M. Ebadi, A. A. Tahir, J. S. Sagu and M. A. Mat Teridi, *J. Phys. Chem. C*, 2017, **121**, 6218–6228.
100 W. Wang, P. J. Strohbeen, D. Lee, C. Zhou, J. K. Kawasaki, K.-S. Choi, M. Liu and G. Galli, *Chem. Mater.*, 2020, **32**, 2899–2909.
101 J. Shi, W. Zhang and Q. Gu, *J. Phys. Chem. C*, 2022, **126**, 9541–9550.
102 J. Li, H. Yuan, J. Li, W. Zhang, Y. Liu, N. Liu, H. Cao and Z. Jiao, *Appl. Catal., B*, 2021, **285**, 119833.
103 C. Regmi, Y. K. Kshetri, D. Dhakal, J. K. Sohng, F. Rosei and S. W. Lee, *Appl. Surf. Sci.*, 2019, **466**, 787–800.
104 Z. Zhao, W. Luo, Z. Li and Z. Zou, *Phys. Lett. A*, 2010, **374**, 4919–4927.
105 J. Zhang, M. Deng, F. Ren, Y. Wu and Y. Wang, *RSC Adv.*, 2016, **6**, 12290–12297.
106 H. S. Park, K. E. Kweon, H. Ye, E. Paek, G. S. Hwang and A. J. Bard, *J. Phys. Chem. C*, 2011, **115**, 17870–17879.
107 M. Yu, Y. Tang, Y. Liao, W. He, X. Lu and X. Li, *J. Mater. Sci. Technol.*, 2023, **165**, 225–234.
108 T. A. Mahi, Q. S. Hossain, S. S. Nishat, S. Ahmed, M. N. I. Khan, M. S. Bashar, S. A. Jahan, U. S. Akhtar, S. Jahan, F. Chowdhury, K. S. Hossain, A. Irfan and I. Ahmed, *Heliyon*, 2024, **10**, e29408.
109 I. Laraib, M. A. Carneiro and A. Janotti, *J. Phys. Chem. C*, 2019, **123**, 26752–26757.